Microscopic theory of polarization properties of optically anisotropic vertical-cavity surface-emitting lasers

D. Burak,[1,*] J. V. Moloney,[2] and R. Binder[1]
[1]*Optical Sciences Center, University of Arizona, Tucson, Arizona 85721*
[2]*Arizona Center for Mathematical Sciences, Department of Mathematics, University of Arizona, Tucson, Arizona 85721*
(Received 1 March 1999; published 13 April 2000)

The polarization eigenmodes of vertical-cavity surface-emitting lasers (VCSELs) are investigated theoretically. The study is based on a first-principles theory and includes a microscopic model for the optically active quantum well and a vectorial solution of the VCSEL cavity mode problem. The theory is evaluated for an anisotropically strained GaAs quantum well structure, interacting with two orthogonally polarized VCSEL eigenmodes. The dependence of the calculated input-output characteristics and polarization stability criteria on microscopic input parameters such as the value of the strain are discussed for various levels of sophistication of the microscopic many-body effects used in the analysis. The results of the stability analysis are consistent with recent experimental observations of polarization switching, suggesting that anisotropic strain of the active quantum well may be a dominant factor in those observations.

PACS number(s): 42.55.Px, 42.55.Sa

I. INTRODUCTION

Due to their rapidly increasing importance in commercial applications, vertical-cavity surface-emitting lasers (VCSELs) are currently the subject of numerous experimental and theoretical investigations (for a recent comprehensive review of VCSEL properties see, e.g., Ref. [1]). Cylindrically symmetric VCSELs offer beam shapes that make them clearly advantageous in comparison to conventional edge emitting lasers, but, on the other hand, they exhibit polarization instabilities in the input-output characteristics [2–6], which is a limiting factor in polarization-sensitive applications, such as optical interconnects, optical communication, optical signal processing, and magneto-optic memories. Efforts have been made to control the polarization by use of anisotropic cavity geometry [7,8], amorphous [9] or metal/dielectric [10] gratings on the top mirror, trench etching [11], cavity tilting [12], fractional-layer superlattices [13], anisotropic oxide aperture [14], external uniaxial strain applied to the structure [15], and optically active quantum wells grown on misoriented substrates [16]. Also, quantum wire [17] and quantum dot [18] VCSELs have been demonstrated to exhibit relatively good polarization selectivity. Most of these approaches, however, require usually some additional regrowth or implantation, which may make the commercial production of these structures more difficult.

It has been demonstrated experimentally that practical VCSELs emit linearly polarized light with preference of the polarization direction along the $[110]$ or $[1\bar{1}0]$ crystallographic axes [2,3,19,20]. Depending on the operating conditions, like pumping current and temperature, bistability between two linearly polarized states of the same fundamental Gaussian-like transverse mode has been demonstrated [3,20]. The preference for a particular polarization indicates the presence of residual anisotropies in the structure, which may result from unintentional residual strain left after the growth process. As a matter of fact, it is possible by applying, for example, additional strain (via the ''hot-spot technique'' [21] or ''local burning'' [22]) to manipulate the dominant birefringence anisotropy at will (i.e., to cancel or magnify it) and therefore to control the output polarization state of light. In these experiments the anisotropy due to dichroism was found to be much smaller than that due to birefringence. A simplified coupled-mode model, based on a combination of linear anisotropies and polarization eigenmode properties, was proposed to obtain phenomenological explanations of observed phenomena [23].

However, from a theoretical point of view, semiconductor lasers are nonlinear systems, where nonlinear gain dispersion and saturation plays a significant role in the mode selection processes. The first, simplified, VCSEL model that accounts for these effects in a phenomenological way was proposed by San Miguel, Feng, and Moloney (SFM) [24]. Underlying that theory is the assumption that the dynamics of optically anisotropic VCSELs can be described by rate equations, where the cavity can be assumed to be uniform in the transverse direction and the optical response of the material can be modeled by the interaction of two coupled two-level systems. Because of its simplicity, this model allows for the prediction of the basic dynamical behavior of the system as a function of the phenomenological input parameters. In this way a number of issues have been addressed, including polarization instabilities and polarization state selection [24,25], the influence of magnetic field on polarization dynamics [26], the role of the various type of optical anisotropies on polarization selection [27], noise-induced polarization hopping and the role of carrier dynamics in this process [28], and the influence of quantum noise on polarization fluctuation [29]. The predictive potential of this approach has been recently confirmed in the context of polarization switching [30,31,6]. Also, polarization dynamics of VCSELs including the onset and the polarization of higher-order modes has been studied [32–34].

*Present address: Agilent Technologies, 350 W. Trimble Rd., MS 90UB, San Jose, CA 95131.

Despite the success in predicting polarization selection and switching phenomena, the above mentioned models did not account for three important aspects of VCSEL structures. The first aspect is that in a semiconductor laser, as already recognized in Ref. [24], the optical transitions take place between electrons in conduction and holes in valence bands, with Coulomb interactions modifying the strength of these transitions [35] (a generalization of the SFM model to the case of a microscopically calculated linewidth enhancement factor, within the free-carrier approximation, has been presented in Ref. [36]). Under many realistic conditions, nonequilibrium many-body effects can be observed in the emission characteristics [37,38], especially under ultrashort excitation conditions. Thus a microscopic description of VCSELs is necessary in order to fully understand its complicated spatiospectral dynamics (see Refs. [39,40] and references therein). The microscopic description is also required to formulate a self-consistent approach to temperature effects [41] and to understand their role in spatiotemporal pattern formation [42]. In addition to Coulomb interactions, semiconductor quantum wells contain specific band-structure effects. In a GaAs quantum well, for example, band-mixing effects yield momentum-dependent optical selection rules. This effect cannot be incorporated into a two-level model. These two additional coupling mechanisms modify the properties of polarization eigenmodes, and therefore, can modify significantly the results of the recently proposed method for an estimation of spin-flip relaxation rates in VCSELs [43]. The model developed in this paper allows us to study the properties and stability of polarization eigenmodes of VCSELs with microscopic effects of band-mixing and Coulomb interactions between the electron and the hole plasma taken into account in a self-consistent way.

The second aspect that needs to be considered in a systematic way is of purely electromagnetic nature and concerns the role played by the distributed Bragg reflectors (DBRs) in mode formation and selection phenomena, especially if higher-order modes of index-guided (or oxide) cavities are considered. One should point out that for index-guided (or oxide) cavities one cannot use the scalar or LP mode approximation, as it is common practice for gain-guided cavities, since only full vectorial hybrid modes satisfy all the necessary boundary conditions in the transverse direction in each cavity layer. Therefore only the solutions of the vector-Maxwell equations characterize properly the three-dimensional (3D) vectorial pattern, eigenfrequencies, and modal losses (including diffraction and scattering loss). Such vectorial solutions have been obtained recently by means of plane-wave expansions [44], general mode expansions [45], vectorial weighted index [46], hybrid mode expansion [47,48], finite-element method [49], and finite difference time domain [50] techniques. In this paper we incorporate the vectorial nature of cold-cavity eigenmodes of realistic VCSEL structures [47,48] into the polarization-sensitive many-body microscopic description of a running laser (the preliminary model including only the free-carrier description of a semiconductor quantum well has been presented in Ref. [51]).

The third aspect that will be discussed in this paper is the origin of optical anisotropies. A potential source of the optical anisotropy of VCSELs is unintentional anisotropic strain. For simplicity, we assume that the dominant anisotropic effects are created by the active layer, which consists of a spacer and a quantum well (QW). Then we apply the theory of uniaxially strained QWs [52–56], which has been generalized to include many-body effects [57,58] and evaluated for the case of ultrashort pulse propagation in Ref. [59]. In this paper we derive the analytical expression for the steady-state susceptibility tensor of anisotropic QWs that is valid for high-quality VCSEL structures. In order to analyze the stability properties of VCSEL polarization eigenmodes one needs to know the steady-state response function of a quantum well. The direct time integration of evolution equations, as it is a common practice in existing microscopic models of VCSELs [37,38,40], would lead only to stable solutions, leaving the unstable solutions out of the analysis.

Within the SFM model one can understand switching from one polarization eigenstate to another by studying its stability properties: If one eigenstate becomes unstable then, as a result of internal fluctuations, the laser output switches to another state [24,25,27]. The physical mechanism proposed to explain polarization switching in systems with dominant birefringence [6,30] is that (in addition to residual linear anisotropies) nonlinear anisotropies arise as a result of an effective frequency shift of the nonlasing mode. At some pumping level the frequency of the nonlasing mode overlaps with that of the lasing mode, which then enables switching. Another mechanism of polarization switching was demonstrated in terms of heating of the device and the resulting shifts in the relative tuning of the cavity resonance with respect to the semiconductor gain spectrum [19,20]. It is beyond the scope of this paper to answer the question of which of these mechanisms is dominant in practical VCSEL structures. We would like to emphasis that the theory presented in this paper lays the foundation for future investigations including self-consistent incorporation of thermal effects [41] into the analysis and for a study of the role of nonlinear anisotropies and heating on polarization switching simultaneously.

This paper is organized as follows. Section II contains the details of the VCSEL structure considered in this paper and the model equations used for analysis. Section III contains the results of strain-induced steady-state refractive index and gain anisotropies in QWs. The input-output (I/O) characteristics of VCSELs operating in the linearly polarized mode regime and their stability properties are discussed in Secs. IV and V, respectively. The physical mechanism leading to polarization switching is discussed in Sec. VI. Section VII summarizes the paper. In Appendices A and B we present details of the derivations of the optical and electronic parts of our model, respectively.

II. MODEL EQUATIONS OF ANISOTROPIC VCSELS

As mentioned in the Introduction, in order to study the polarization properties of anisotropic VCSELs one should develop a model that takes into account the dynamics of vectorial eigenmodes of realistic structures coupled to the

dynamics of electrons and holes in QW bands. In this section we present a set of simplified equations describing the time evolution of the electromagnetic fields and carrier densities in anisotropic VCSELs. In the most general case one should consider a multitransverse-mode field dynamics coupled to spatiospectral evolution of carrier densities, which describes a polarization-dependent mode selection processes due to the spatial (modal gain overlap) and spectral (modal gain supression) hole burning. For the case of anisotropic quantum wells such equations are derived in Appendices A and B for fields and carrier densities, respectively. However, in this paper we focus on a simplified case of a small-diameter VCSEL operating close to the lasing threshold, which allows us to limit the analysis to the case of two fundamental, orthogonally polarized modes. Thus one can neglect the effects of spatial hole burning and the appropriate equations are presented in Sec. II B.

A. The cavity structure

We begin our study by considering a cylindrical air-post index-guided cos-type λ cavity grown on a GaAs substrate and designed to be at resonance at $\lambda_0 \approx 0.851$ μm. The room-temperature material parameters are taken from Ref. [60]. The central, optically active part of the cavity consists of a λ-thick spacer layer of $Al_{0.05}Ga_{0.95}As$ barrier material with refractive index $n_S = 3.658$ and a $L_{QW} = 10A$-thick GaAs quantum well. We neglect the small change of the average refractive index due to the presence of the thin QW layer. The front mirror consists of a distributed Bragg reflector (DBR) with $N_F = 26$ pairs of $Al_{0.3}Ga_{0.7}As/AlAs$ layers with $n_L = n_{AlAs} = 2.99$ (low) and $n_H = n_{Al_{0.3}Ga_{0.7}As} = 3.47$ (high) refractive indices. The rear DBR consists on $N_R = 34$ pairs of layers. Note that $N_R > N_F$, which prevents the leakage of light into the substrate. The cavity radius is assumed to be $R = 2$ μm, which leads to the modified resonant wavelength (due to cavity-induced blue shift, see Ref. [48]) for the fundamental HE_{11} eigenmode $\lambda_R^{HE_{11}} \approx 0.849$ μm and the photon life-time $\tau_{phot}^{HE_{11}} \approx 1.46$ ps.

B. Model equations for optical fields and carrier densities

The optical characterization of the VCSEL structure described in Sec. II A involves finding a complete set of vectorial eigenmodes directly from Maxwell equations. The theory of cold-cavity vectorial eigenmodes of index-guided VCSELs has been presented in Refs. [47,48]. In this section we present results of the application of this theory to the running laser. Within the two-mode approximation, the evolution equations for the field amplitudes inside the quantum-well layer are given by (see Appendix A for details of the derivation)

$$\frac{dA_x}{dt} = \omega_e[\chi_B^{HE_{11}\prime\prime} A_x + i(\chi_{QW}^{xx} A_x - \chi_{QW}^{xy} A_y)], \tag{1}$$

$$\frac{dA_y}{dt} = \omega_e[\chi_B^{HE_{11}\prime\prime} A_y + i(-\chi_{QW}^{yx} A_x + \chi_{QW}^{yy} A_y)], \tag{2}$$

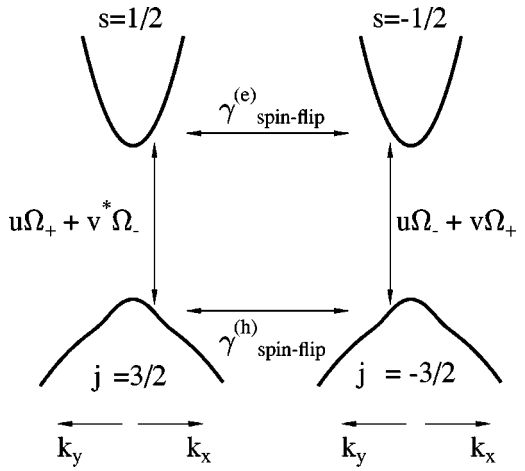

FIG. 1. Schematic of the in-plane band structure of a quantum well [k_x and k_y indicate $(k_x,0)$ and $(0,k_y)$ directions in reciprocal space, respectively]. Shown are two conduction bands ($\pm 1/2$) and two valence bands ($\pm 3/2$). $\Omega_\pm$ denotes $\mu \vec{e}_\pm \cdot \vec{E}$, see Eqs. (B5) and (B7), and both spin subsystems are coupled via spin-flip relaxation rates of electrons $\gamma_{spin\text{-}flip}^{(e)}$ and of holes $\gamma_{spin\text{-}flip}^{(h)}$. The transformation elements u and v are defined in the text.

where $A_{x/y}$ is the field amplitude of x/y polarized fundamental hybrid HE_{11} mode, $\omega_e = 2\pi\omega_0/(1+4\pi\chi_B)$, ω_0, and $\chi_B^{HE_{11}''}$ denote the cold-cavity frequency and modal loss of the HE_{11} mode, respectively, χ_B is a background susceptibility of the quantum well material, and χ_{QW}^{ij}, $(i,j = x,y)$ are the elements of the susceptibility tensor describing optical gain and electronic contributions to the refractive index of anisotropically strained quantum wells.

The polarization-dependent optical gain in semiconductors is determined by lasing transitions between conduction and valence bands. The band structure near the band gap can be calculated using the **k·p** Luttinger-Kohn theory [57,61]. The conduction and the valence bands can be classified according to the value of the effective total angular momentum J. Spin 1/2 electrons occupy the conduction bands with total angular momentum $J = 1/2$ (here the orbital angular momentum is zero), whereas holes can occupy three different valence bands: heavy-hole (hh) and light-hole (lh) band, both with angular momentum $J = 3/2$, and the split-off band with angular momentum $J = 1/2$. Because the split-off band has a much lower energy than the hh and lh bands, it can be disregarded in the analysis. The hh and lh band are degenerate at zero momentum in bulk semiconductors. However, in quantum wells the 3D translation symmetry is broken, which leads to a splitting between hh and lh bands: the hh band associated with $j = \pm 3/2$ (where j is the z component of the angular momentum) has a higher energy at zero momentum. The schematics of the quantum well band structure and optical transitions connecting the conduction and valence bands considered in this paper is shown in Fig. 1. We assume that the quantum well is thin enough so that only the lowest subband of each band has to be taken into account. The optical transitions at the zone center are associated with circularly polarized electric field components and are indicated by $\Omega_\pm$. The change of the valence band curvature is due to

band-mixing effects described by the Luttinger Hamiltonian. Additionally, the coupling between both spin subsystems due to spin-flip relaxation interactions has been indicated by horizontal lines. In this paper we incorporate phenomenologically the spin-flip relaxation processes to the semiconductor Bloch equations within the relaxation rate approximation.

The optical response of quantum well is determined by the time evolution equations for in-plane momentum resolved distribution functions describing electrons (superscript e) in the conduction (subscripts $\pm 1/2$) and holes (superscript h) in the heavy-hole (subscripts $\pm 3/2$ and a ''tilde'' over f) bands, which are given by (see Appendix B for details of the derivation)

$$\frac{d}{dt} f^{e}_{\pm 1/2,\pm 1/2} = -\gamma^{e}_{R} f^{e}_{\pm 1/2,\pm 1/2} - \gamma^{e}_{S}(f^{e}_{\pm 1/2,\pm 1/2} - f^{e}_{\mp 1/2 \mp 1/2}) - \gamma^{e}_{F}(f^{e}_{\pm 1/2,\pm 1/2} - n^{e}_{\pm 1/2}) + \left(\frac{d}{dt} f^{e}_{\pm 1/2,\pm 1/2}\right)_{p} + \left(\frac{d}{dt} f^{e}_{\pm 1/2,\pm 1/2}\right)_{s} \tag{3}$$

$$\frac{d}{dt} \tilde{f}^{h}_{\pm 3/2,\pm 3/2} = -\gamma^{h}_{R} \tilde{f}^{h}_{\pm 3/2,\pm 3/2} - \gamma^{h}_{S}(\tilde{f}^{h}_{\pm 3/2,\pm 3/2} - \tilde{f}^{h}_{\mp 3/2 \mp 3/2}) - \gamma^{h}_{F}(\tilde{f}^{h}_{\pm 3/2,\pm 3/2} - n^{h}_{\pm 3/2}) + \left(\frac{d}{dt} \tilde{f}^{h}_{\pm 3/2,\pm 3/2}\right)_{p} + \left(\frac{d}{dt} \tilde{f}^{h}_{\pm 3/2,\pm 3/2}\right)_{s}. \tag{4}$$

The meaning of the various terms in Eqs. (3)–(4) is as follows: γ^{α}_{R} ($\alpha = e/h$) is the recombination rate describing nonradiative processes, γ^{α}_{S} is the spin-flip relaxation rate, $\gamma^{\alpha}_{F} = \hbar/T_2$ is the carrier-carrier scattering rate and describes relaxation of actual carrier distributions towards corresponding Fermi distributions $n^{\alpha}_{\pm i/2}$, which are normalized such that

$$\sum_{\vec{k}} \tilde{f}^{\alpha}_{\pm i/2,\pm i/2}(\vec{k}) = \sum_{\vec{k}} n^{\alpha}_{\pm i/2}(\vec{k}). \tag{5}$$

The pumping term, which takes into account heating of carriers due to Pauli blocking, is given by [38]

$$\left(\frac{d}{dt} \tilde{f}^{\alpha}_{\pm i/2,\pm 1/2}\right)_{p} = \frac{j \eta^{\alpha}_{\pm i/2}}{e} \frac{F^{\alpha}(1 - f^{\alpha}_{\pm i/2,\pm i/2})}{1/L^2 \sum_{k} F^{(\alpha)}}, \tag{6}$$

where j is a pumping current, $\eta^{\alpha}_{\pm 1/2}$ is the pumping efficiency, normalized such that the amount of electrons and holes entering the active region per unit time is the same, F^{α} is a Fermi distribution representing the pumped carriers. Throughout this paper we used distributions F^{α} corresponding to the pumping carrier density $1 \times 10^{13}/\mathrm{cm}^2$ (a detailed discussion of how the pumping density influences lasing characteristics can be found in Ref. [38]). Each term in Eqs. (3)–(4) is $\vec{k}$ resolved, but this index has been suppressed for simplicity. More details on how one can introduce phenomenologically these terms to the original set of Eqs. (B2) for the case of a two-band single-mode laser model can be found, e.g., in Ref. [57].

The stimulated emission term is given by

$$\left(\frac{d}{dt} \tilde{f}^{h}_{\pm 3/2,\pm 3/2}(\vec{k})\right)_{s} = \frac{|\mu|^2 \Gamma_R}{2\hbar} \mathrm{Im}\Big([1 + \mathcal{G}^{*}_{\pm 1/2}(\mathcal{F}_{\pm 1/2}; -\vec{k})] \times \frac{\mathcal{F}_{\pm 1/2}(-\vec{k})}{1 - \mathcal{G}_{\pm 1/2}(\mathcal{F}_{\pm 1/2}; -\vec{k})} [\chi^{xx\pm}_{QW}(\vec{k})|A_x|^2 - \chi^{xy\pm}_{QW}(\vec{k}) A^{*}_{x} A_y - \chi^{yx\pm}_{QW}(\vec{k}) A_x A^{*}_{y} + \chi^{yy\pm}_{QW}(\vec{k})|A_y|^2] \Big), \tag{7}$$

and a similar relation for $f^{e}_{\pm 1/2,\pm 1/2}$, where μ is the magnitude of the macroscopic Cartesian dipole matrix element and Γ_R is the modal field overlap factor. The free-carrier ($\mathcal{F}$) and the local field ($\mathcal{G}$) correction factors are calculated within the (0-1) Padé approximation as

$$\mathcal{F}_{\pm 1/2}(\vec{k}) = \frac{1 - f^{e}_{\pm 1/2,\pm 1/2}(\vec{k}) - \tilde{f}^{h}_{\pm 3/2,\pm 3/2}(\vec{k})}{-\frac{i\hbar}{T_2} + \varepsilon^{s}_{k} + E_{hh}(\vec{k}) - \Sigma_{\pm 1/2}(\vec{k}) - \hbar\omega_0}, \tag{8}$$

$$\mathcal{G}_{1/2}(\mathcal{F}_{1/2}; \vec{k}) = \sum_{\vec{q}} V(\vec{q}) [u(\vec{k}) u(\vec{k} + \vec{q}) + v^{*}(\vec{k}) v(\vec{k} + \vec{q})] \mathcal{F}_{1/2}(\vec{k} + \vec{q}), \tag{9}$$

$$\mathcal{G}_{-1/2}(\mathcal{F}_{-1/2}; \vec{k}) = \sum_{\vec{q}} V(\vec{q}) [u(\vec{k}) u(\vec{k} + \vec{q}) + v(\vec{k}) v^{*}(\vec{k} + \vec{q})] \mathcal{F}_{-1/2}(\vec{k} + \vec{q}),$$

where the electron energies are parabolic, $\varepsilon^{s}_{k} = \hbar^2 k^2/2m_e + E'_g$, with E'_g being the effective band gap, and the band-gap renormalization $\Sigma_{\pm 1/2}(\vec{k})$ is given by

$$\Sigma_{\pm 1/2}(\vec{k}) = \sum_{\vec{q}} V(\vec{q}) [f^{e}_{\pm 1/2,\pm 1/2}(\vec{k} + \vec{q}) + \tilde{f}^{h}_{\pm 3/2,\pm 3/2}(-\vec{k} + \vec{q}) \times |u(\vec{k}) u(-\vec{k} + \vec{q}) + v(\vec{k}) v^{*}(-\vec{k} + \vec{q})|^2]. \tag{10}$$

The Coulomb potential $V(\vec{q})$ is taken to be the statically screened Coulomb potential in two dimensions [57]. The susceptibility tensor elements $\chi^{\pm}_{QW}(\omega_0)$ describing the nonlinear response of the strained quantum well are

$$\hat{\chi}_{QW}=\frac{|\mu|^2}{2}\sum_{\vec{k}}\left[\hat{\chi}^{+}_{QW}(\vec{k})\frac{\mathcal{F}_{1/2}(\vec{k})}{1-\mathcal{G}_{1/2}(\mathcal{F}_{1/2};\vec{k})}+\hat{\chi}^{-}_{QW}(\vec{k})\frac{\mathcal{F}_{-1/2}(\vec{k})}{1-\mathcal{G}_{-1/2}(\mathcal{F}_{-1/2};\vec{k})}\right], \tag{11}$$

where

$$\chi^{xx+}_{QW}(\vec{k})=\left|u(\vec{k})-\frac{v(\vec{k})}{\sqrt{3}}\right|^2=\chi^{xx-}_{QW}(\vec{k}), \tag{12}$$

$$\chi^{xy+}_{QW}(\vec{k})=i\left[u(\vec{k})-\frac{v(\vec{k})}{\sqrt{3}}\right]\left[u(\vec{k})+\frac{v^*(\vec{k})}{\sqrt{3}}\right]=\chi^{yx-}_{QW}(\vec{k}),$$

$$\chi^{yx+}_{QW}(\vec{k})=-i\left[u(\vec{k})+\frac{v(\vec{k})}{\sqrt{3}}\right]\left[u(\vec{k})-\frac{v^*(\vec{k})}{\sqrt{3}}\right]=\chi^{xy-}_{QW}(\vec{k}),$$

$$\chi^{yy+}_{QW}(\vec{k})=\left|u(\vec{k})+\frac{v(\vec{k})}{\sqrt{3}}\right|^2=\chi^{yy-}_{QW}(\vec{k}).$$

The details of the band structure of the quantum well are taken into account via the momentum- $(\vec{k})$ dependent coefficients

$$u(\vec{k})=\frac{H_{lh}(\vec{k})-E_{hh}(\vec{k})}{\sqrt{[H_{lh}(\vec{k})-E_{hh}(\vec{k})]^2+|c(\vec{k})|^2}},$$
$$v(\vec{k})=\frac{-c(\vec{k})}{\sqrt{[H_{lh}(\vec{k})-E_{hh}(\vec{k})]^2+|c(\vec{k})|^2}}, \tag{13}$$

where the heavy- $[E_{hh}(\vec{k})]$ and the light-hole $[E_{lh}(\vec{k})]$ eigenenergies are given by

$$E_{hh}(\vec{k})=\frac{1}{2}\{H_{hh}(\vec{k})+H_{lh}(\vec{k})-\sqrt{[H_{hh}(\vec{k})-H_{lh}(\vec{k})]^2+4|c(\vec{k})|^2}\}, \tag{14}$$

$$E_{lh}(\vec{k})=\frac{1}{2}\{H_{hh}(\vec{k})+H_{lh}(\vec{k})+\sqrt{[H_{hh}(\vec{k})-H_{lh}(\vec{k})]^2+4|c(\vec{k})|^2}\}.$$

Finally, the heavy-hole $[H_{hh}(\vec{k})]$, light-hole $[H_{lh}(\vec{k})]$, and coupling $[c(\vec{k})]$ matrix elements, which enter the Luttinger Hamiltonian, are given by

$$H_{hh}(\vec{k})=(\hbar^2/2m_0)(\gamma_1+\gamma_2)(k_x^2+k_y^2)-(1/2)\Delta E_s'(1-2\gamma_s), \tag{15}$$

$$H_{lh}(\vec{k})=(\hbar^2/2m_0)(\gamma_1-\gamma_2)(k_x^2+k_y^2)+\Delta_{hh-lh}+(1/2)\Delta E_s'(1-2\gamma_s),$$

$$c(\vec{k})=-(\hbar^2/2m_0)\sqrt{3}[\gamma_2(k_x^2-k_y^2)-2i\gamma_3 k_x k_y]+(\sqrt{3}/2)\Delta E_s.$$

The Luttinger parameters are γ_1, γ_2, γ_3, and the strain contributions $\Delta E_s'=b_s(e_{xx}+e_{yy})$, $\Delta E_s=b_s(e_{xx}-e_{yy})$, with $\gamma_s=S_{12}/(S_{11}+S_{12})$, contain the elastic compliances S_{11} and S_{12}, the shear deformation potential b_s, and the strain tensor elements e_{xx} and e_{yy}. The hydrostatic stress component, which renormalizes the band-gap energy by the amount

$$\delta E_{hydr}=b_{hydr}(e_{xx}+e_{yy}+e_{zz}),\quad e_{zz}=\gamma_s(e_{xx}+e_{yy}), \tag{16}$$

as well as the quantum confinement energy, has been put into the definition of E_g' and, therefore, does not occur explicitly. The hh-lh splitting is denoted by Δ_{hh-lh}. The numerical values for the material parameters are $m_e=0.067m_0$, $\gamma_1=6.85$, $\gamma_2=2.1$, $\gamma_3=2.9$, $\Delta_{hh-lh}=30$ meV, $b_s=-1.7$ eV, $b_{hydr}=-8.23$ eV, $S_{11}=1.17\times10^{-3}$ kbar^{-1}, $S_{12}=-0.37\times10^{-3}$ kbar^{-1}, $e_{yy}=0$. Throughout this paper we use the strain tensor element e_{xx} as a parameter that determines the gain and refractive index anisotropy of quantum well.

III. EFFECTS OF UNIAXIAL STRAIN ON INDEX AND GAIN ANISOTROPY

In recent years strain effects in semiconductors have been intensively explored in order to improve the quantum well laser characteristics [61,62]. It is known that, for example, biaxial compressive strain reduces the hole effective mass, thus reducing the density of states and (for a certain range of carrier densities) increasing the gain. However, as a function of carrier density, the gain of the strained quantum well saturates sooner and at lower values than for an unstrained QW (see, e.g., Fig. 10.28b in Ref. [61]).

As already mentioned in the Introduction, in this paper we are mainly interested in the effect of unintentional uniaxial strain on VCSEL characteristics. To simplify the calculations, we assume that the strain is uniform in the plane of the quantum well. In general, unintentional strain will be different in different devices, with specific transverse and longitudinal spatial dependencies that are determined by the details of the fabrication process. To model the principle effects of strain in a generic device-independent way, we use a very simple spatial strain distribution model, namely, transversely homogeneous strain located only in the active quantum well.

We begin by showing in Fig. 2(a) the anisotropic transform matrix elements u and v (left-hand side axis) that determine the mixing between left and right polarized light components for optical transitions within each spin subsystem, evaluated for a uniaxial compressive strain in the x direction, $e_{xx}=-0.05\%$. For comparison, the anisotropic (isotropic) distribution functions for holes (electrons) obtained for a total carrier density $N\approx1.36\times10^{12}$ cm^{-2} is also shown. Note that lasing action usually takes place close to the bottom of the bands, where the anisotropy is largest.

In Fig. 2(b) we show the polarization-resolved anisotropic

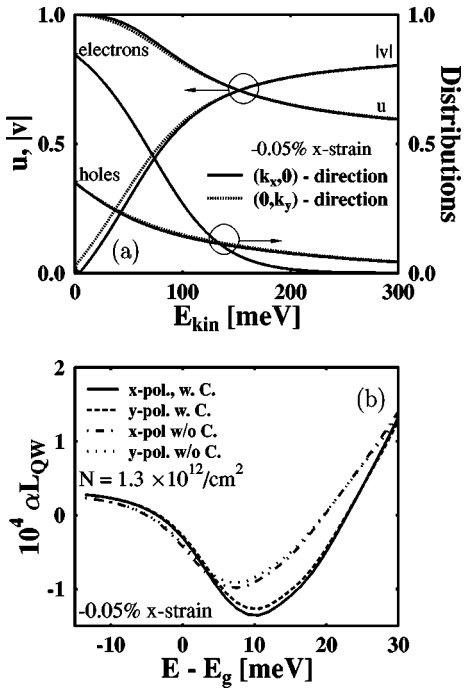

FIG. 2. (a) Left-hand axis: anisotropic elements of the transformation matrix $\mathcal{U}(\vec{k})$, see Eq. (B9), as a function of kinetic energies of electrons and holes in the corresponding bands. Right-hand axis: Fermi-Dirac distribution functions for electrons and holes for a carrier density of $N \approx 1.3\times 10^{12}$ cm^{-12}. A compressive strain in the x direction $e_{xx}=-0.05\%$ is assumed and results are shown for $(k_x,0)$ (solid line) and $(0,k_y)$ (dots). (b) Dimensionless gain calculated for a strained QW ($e_{xx}=-0.05\%$) and carrier density $N=1.3\times 10^{12}$ cm^{-12} using the many-body (w. C.) and free-carrier (w/o C.) models, respectively.

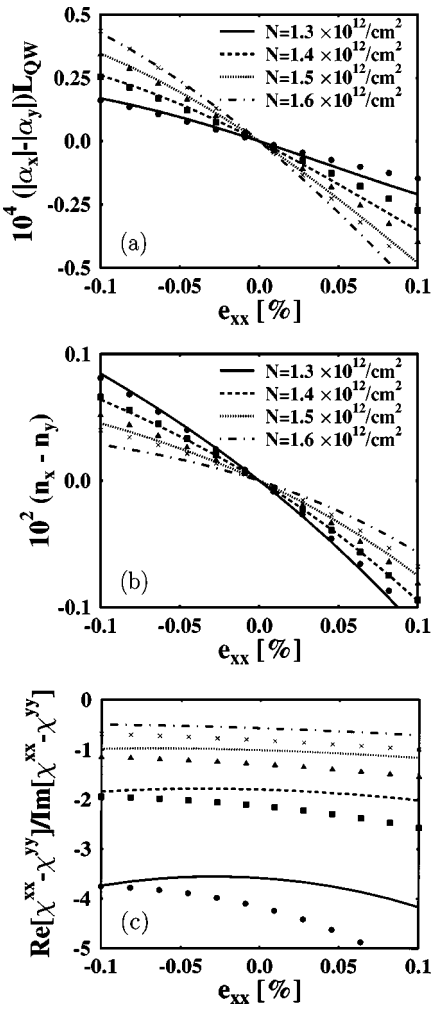

FIG. 3. (a) Gain dichroism, (b) birefringence, and (c) relative ratio between dichroism and birefringence for a strained quantum well for various carrier densities as a function of uniaxial strain, calculated for the model with Coulomb interactions (lines). Circles, squares, triangles, and crosses correspond to results obtained from the free-carrier model for densities $N=1.3$, 1.4, 1.5, and 1.6 $\times 10^{12}$ cm^{-2}, respectively. The results are shown for the functions evaluated at the lasing frequency ω_0.

steady-state gain spectra for density $N=1.3\times 10^{12}$ cm^{-2} and strain $e_{xx}=-0.05\%$. We solved Eqs. (A10)–(A11) in order to obtain the values of the effective refractive index n_{eff} and dimensionless gain $\alpha_{x/y}L_{QW}$ [see the discussion following Eq. (A11)] as a function of the susceptibility tensor elements $\chi_{QW}^{x/y,x/y}$ [see Eq. (11)]. One can clearly see the gain difference (dichroism) for x- and y-polarized light around the gain maximum. For comparison, we show also the gain anisotropy as calculated by using the free-carrier model, i.e., by neglecting the Coulomb enhancement effects, $\mathcal{G}_{\pm 1/2}=0$. However, in order to allow for a fair comparison, we kept the renormalized band gap, Eq. (10), evaluated at the bottom of the bands, $\Sigma_{\pm 1/2}(\vec{k}=0)$, which introduces the frequency redshift to the spectrum. The overall free-carrier spectrum is then redshifted in comparison to the many-body spectrum since $\Sigma_{\pm 1/2}(0)\leqslant\Sigma_{\pm 1/2}(\vec{k})<0$. The Coulomb interaction modifies the shape and value of the gain curve in a similar way to what was reported for isotropic QWs [57].

For an understanding of the polarization selection and switching in VCSELs it is crucial to know the strain induced dichroism and birefringence of the QW. Figure 3 shows these quantities, evaluated at the laser frequency ω_0, as a function of uniaxial strain e_{xx} and carrier density N. For comparison, we show results calculated from both many-body and free-carrier models. As already indicated by Fig. 2(b), the compressive strain (negative e_{xx}) leads to larger gain for x-polarized light, $|\alpha_x|>|\alpha_y|$ [Fig. 3(a)]. For tensile strain (positive e_{xx}) the opposite behavior occurs. Of course, the gain dichroism increases with increasing strain. Also, as one increases the carrier density, the gain dichroism is found to increase as well. Note that for the configuration presented here (fixed laser frequency), the free-carrier model underestimates the value of the gain difference.

The strain induced birefringence is shown in Fig. 3(b). Similar to the gain dichroism, the birefringence increases with increasing strain. However, it decreases with increasing density. We also see that the free-carrier model underestimates the value of the birefringence for densities around $N=1.3\times 10^{12}$ cm^{-2} and overestimates it for larger densities (see, for instance, the result for $N=1.6\times 10^{12}$ cm^{-2}). The ratio of birefringence to dichroism, one of the parameters that determines the stability properties of VCSEL eigen-

modes, is shown in Fig. 3(c). For the laser parameters considered in this paper ($N \approx 1.36 \times 10^{12}$ cm^{-2}) the following approximate numerical relation holds: $\mathrm{Re}[\chi_{QW}^{xx} - \chi_{QW}^{yy}] \approx -2.5\,\mathrm{Im}[\chi_{QW}^{xx} - \chi_{QW}^{yy}]$. However, this can change within an order of magnitude, depending on cavity quality, tuning, and/or temperature (not considered in this paper). Note also that the free-carrier model usually overestimates the magnitude of the relative ratio between anisotropies.

IV. STEADY-STATE INPUT-OUTPUT CHARACTERISTICS OF VCSELS

Within the rate-equation approximation, the polarization eigenmodes and polarization dynamics of light in VCSELs has been studied in detail in Refs. [24,25,27,28] for cavities with phenomenologically introduced birefringence and dichroism. It has been found that for the two-mode laser model (modes with the same Gaussian-like transverse pattern) the system has four possible eigenstates: two linearly polarized and two circularly (elliptically) polarized states for isotropic (anisotropic) cavities [25,27,28]. The stability of these modes depends on the laser parameter values. In general, if the principal axes of birefringence and dichroism are aligned, there exists such a parameter range where the linearly polarized modes can be stable. However, if the birefringence and dichroism are misaligned, only the elliptically polarized states were found to be stable [63,64].

In order to find the polarization eigenmodes described by the set of equations (1)–(2) and (3)–(4), we look for steady-state solutions in the form

$$A_x(t) = A_x^0 e^{i\delta t}, \quad A_y(t) = A_y^0 e^{i(\delta t + \varphi)}, \tag{17}$$

where A_x^0 and A_y^0 are real amplitudes, δ describes small modifications of the mode eigenfrequency due to the mode pulling effect, and φ is the phase difference between the electric field vectors in two orthogonal polarizations. Using phenomenological models it was found that, for instance, for linear polarization only one of these amplitudes can be nonzero, whereas for circular polarization (in the case of isotropic cavities only) $A_x^0 = A_y^0$ and $\varphi = \pm \pi/2$, where the signs correspond to polarizations with opposite handednesses. For anisotropic cavities one finds the same type of solutions, but with elliptically polarized eigenmodes (characterized by ellipticity and azimuth angles) replacing circularly polarized ones [25,27,28].

In this paper we will focus only on properties of linearly polarized eigenmodes, as they play a dominant role in realistic VCSEL structures. If the principal axes of birefringence and gain dichroism are aligned (as it is the case in this paper), the elliptically polarized modes are involved only temporarily in the switching process between a mode that loses its stability to its orthogonally polarized mode [31]. The steady-state solutions for linearly polarized modes can be obtained by substituting Eq. (17) into Eqs. (1)–(2). Separating these equations into real and imaginary parts, one obtains the nonlinear condition for mode amplitudes and frequency shifts for x-polarized modes ($A_y = 0$)

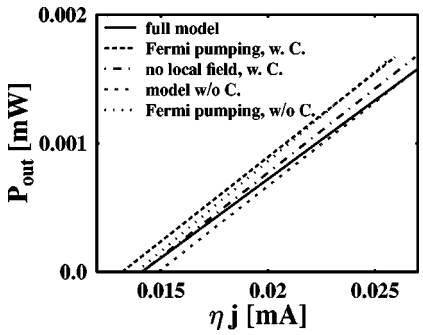

FIG. 4. Input-output characteristics of an optically isotropic VCSEL: full model (solid line), ''Fermi-pumping'' model with Coulomb enhancement effects (dashed line), full model but without the local field effects (dashed-dotted line), free-carrier model (double-dotted line), and free-carrier model with ''Fermi pumping'' (dotted line).

$$\chi_B^{HE_{11''}} = \mathrm{Im}[\chi_{QW}^{xx}], \quad \delta = \frac{2\pi\omega_0}{1 + 4\pi\chi_B}\,\mathrm{Re}[\chi_{QW}^{xx}], \tag{18}$$

and for y-polarized modes ($A_x = 0$)

$$\chi_B^{HE_{11''}} = \mathrm{Im}[\chi_{QW}^{yy}], \quad \delta = \frac{2\pi\omega_0}{1 + 4\pi\chi_B}\,\mathrm{Re}[\chi_{QW}^{yy}]. \tag{19}$$

These equations need to be solved simultaneously with the nonlinear set of Eqs. (3)–(4) under steady-state conditions ($\dot{f}^{e}_{\pm 1/2, \pm 1/2} = \dot{f}^{h}_{\pm 3/2, \pm 3/2} = 0$). Because we are interested in cavities with small unintentional strain induced anisotropies in the thin QW region, the resulting overall change of the cavity birefringence is small. Thus we use the isotropic cold-cavity eigenfrequency ω_0 and cavity loss $\chi_B^{HE_{11''}}$ in our steady-state calculations. In the numerical solutions discussed below we use the following values for decay times (unless otherwise noted): $T_2 = 100$ fs, $(\gamma_S^e)^{-1} = 10$ ps $= (\gamma_S^h)^{-1}$, $(\gamma_R^e)^{-1} = 1$ ns $= (\gamma_R^h)^{-1}$, and $(\gamma_F^e)^{-1} = 100$ fs $= (\gamma_F^h)^{-1}$.

A. Influence of Coulomb effects on laser characteristics

Let us first consider the input-output (IO) characteristics of the isotropic VCSEL ($e_{xx} = 0$). In Fig. 4 we demonstrate how various terms entering Eqs. (3)–(4) contribute to the steady-state IO characteristics. The solid line indicates the model with all terms present. The calculated threshold current in this case is $j^{thr} \approx 14.1$ μA and the slope efficiency is $\kappa \approx 0.12$ W/A. The threshold current for the considered device is about two orders of magnitude smaller than that measured for a real device, because we (i) consider a high-quality, small-area cavity, (ii) neglect optical loss due to free-carrier absorption in the mirrors, and (iii) neglect current leakage in the cavity layers. Phenomenologically, these effects can be included in the pumping efficiency factor η (in this paper $\eta = 1$). On the other hand, the calculated slope efficiency is about two times smaller than typical data presented in the literature [20]. This is because in practical de-

vices one uses rear mirrors with twice as many layers as the front mirrors, which keeps the light from propagating into the substrate.

We can study the role of Pauli blocking in the pumping process, by making an unphysical assumption that electrons and holes are pumped directly into Fermi-Dirac distributions; that is, we replace the pumping term (6) by

$$\left(\frac{d}{dt} f^{\alpha}_{\pm i/2,\pm 1/2}\right)_p = \frac{j\eta^{\alpha}_{\pm i/2}}{e} \frac{n^{\alpha}_{\pm i/2}}{1/L^2 \sum_k n^{\alpha}_{\pm i/2}} . \qquad (20)$$

This leads to a reduction of the threshold current by approximately 7% ($j^{thr} \approx 13.1\ \mu$A) and increase of the slope efficiency to $\kappa \approx 0.131$ W/A (dashed curve in Fig. 4). The reduction of the threshold current is intuitively obvious, as Pauli blocking leads to heating of carriers in the bands [38], which then have to equilibrate before they are available for the lasing process. The process of achieving the thermal equilibrium is described phenomenologically in Eqs. (3)–(4) by the carrier-carrier scattering rate γ^{α}_{F}. Since this is by far the largest rate in the equations, the modifications of the IO due to ''non-Fermi-like'' pumping are rather small.

The next effect that we consider in Fig. 4 is the influence of the local field effects [the term $\mathcal{G}^{*}_{\pm 1/2}(\mathcal{F}_{\pm 1/2}; -\vec{k})$ in the stimulated emission term (7)]. By putting this term to zero, we obtain the same threshold current as for the full model (see Fig. 4, dashed-dotted line), but the slope efficiency is the same (within the numerical accuracy) as for the ''Fermi pumping'' model.

The next modification we consider is the free-carrier model (i.e., we neglected all Coulomb effects except band-gap renormalization, similarly as in Fig. 2). The result is shown in Fig. 4 as the double-dotted line. Because the free-carrier gain is smaller than the many-body gain (no Coulomb enhancement), one has to pump harder in order to compensate for the cavity loss, and therefore the threshold current is increased to $j^{thr} \approx 14.9\ \mu$A (that is by about 5.7% in comparison to the full model). Also, the slope efficiency increased to $\kappa \approx 0.13$ W/A because of lack of local field effects.

The last model is the free-carrier model with ''Fermi pumping'' (Fig. 4, dots), where, again, the threshold current decreases to $j^{thr} \approx 13.8\ \mu$A and the slope efficiency increases to $\kappa \approx 0.14$ W/A. The free–carrier ''Fermi-pumping'' model is the closest to the phenomenological SFM model [24] that assumes the instant thermal equilibration of carriers in the bands (by considering only the Fermi distributions, which allows one to consider total carried densities instead of momentum-resolved carrier distributions).

B. IO characteristics of an anisotropic VCSEL

In this section we focus on the influence of moderate compressive strain ($e_{xx} = -0.01\%$) on the IO characteristics. In Fig. 5(a) we compare the results for *x*- and *y*-polarized eigenmodes. The calculations were done using the full model and the free-carrier model (with band-gap renormalization), both using the pumping term that takes into account the Pauli blocking.

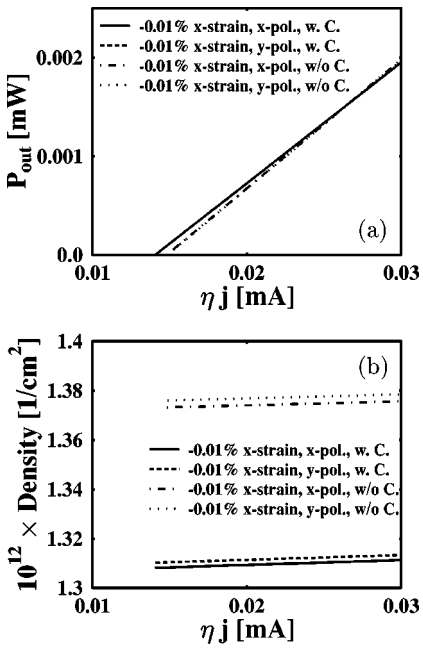

FIG. 5. (a) Input-output characteristics and (b) carrier density vs pumping current for an anisotropic VCSEL with uniaxially strained QW, $e_{xx} = -0.01\%$. Results are obtained from the many-body calculation for *x*-polarized (solid line) and *y*-polarized (dashed line) eigenmodes and from the free-carrier model for *x*-polarized (dashed-dotted line) and *y*-polarized (dotted line) eigenmodes.

As for the model with Coulomb interactions, despite the applied strain, the IO characteristics for both polarizations do not show any visible differences. Since *x*-polarized light experiences more gain in this configuration, the threshold current is about 0.2% smaller than for the *y* polarization. The slope efficiencies differ by about 0.05% between the two polarizations, and so the solid and dashed curves practically overlap in the plot. The results of neglecting the Coulomb effects essentially are the same as described in Sec. IV A. For the free-carrier model one cannot distinguish between IO for both polarizations (dotted and dash-dotted lines are on the top of each other).

In Fig. 5(b) we show how the carrier densities change with the pumping current. Due to the effect of spectral hole burning, one does not observe clamping of the carrier density to the threshold value and so the density increases with increasing current. Since the gain for the *x*-polarized mode is larger than that for *y* polarization, a smaller carrier density is sufficient to generate the same amount of *x*-polarized output power. This yields the difference between operating densities for both polarization eigenstates. As for the free-carrier model, one has to provide a larger amount of carriers to satisfy the gain-equal-loss condition, as it can be seen in Fig. 5(b).

As mentioned above, in our model gain saturation and the resulting spectral hole burning are responsible for changes of carrier densities as a function of pumping current. In Fig. 6(a) we show the differential gain spectra for a laser operat-

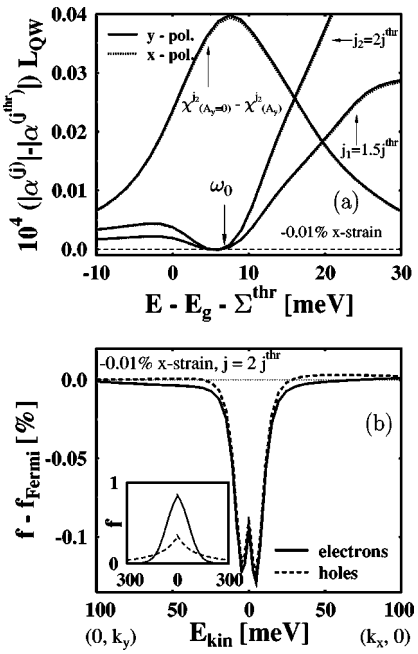

FIG. 6. Spectral characteristics of a laser operating in the *y*-polarized eigenmode. (a) Gain differential spectra for various pumping currents (see text for more details). $\Sigma^{thr} \equiv \Sigma_{\pm 1/2}(\vec{k}=0) \approx 15.8$ meV is the band-gap renormalization calculated for a threshold carrier density of $N \approx 1.36 \times 10^{12}$ cm^{-2}. The arrow labeled ω_0 indicates the position of the lasing mode. (b) Difference between the actual carrier distribution functions f and the corresponding Fermi-Dirac distribution f_{Fermi} for pumping current $j = 2j^{thr}$. The distributions are shown in $(k_x,0)$ direction and in $(0,k_y)$ direction. Inset: Actual distribution functions f.

ing in the *y*-polarized mode. The curve labeled as $j_2 = 2j^{thr}$ ($j_1 = 1.5j^{thr}$) shows the difference between the spectrum calculated for a running laser pumped with the current j_2 (j_1) and the spectrum obtained for a threshold pumping current j^{thr}. Since the carrier density is larger for $j > j^{thr}$ [see Fig. 5(b)], the overall difference between gain spectra is positive. However, at the lasing frequency the gain-equal-loss condition must hold, so the gain values at this frequency are the same. This results in a hole seen in the differential gain spectra. It is interesting to note that even though the *y*-polarized mode is lasing, the spectral hole is the same for both, the active and the inactive mode. This is because of the isotropic nature of the large carrier-carrier scattering rate assumed in our calculations. The last two curves, labeled $\chi^{j_2}_{(A_y=0)} - \chi^{j_2}_{(A_y)}$, show the difference between spectra calculated for a QW for the carrier density obtained for pumping current j_2 without light field ($A_y = 0$, that with carrier distributions taken to be Fermi distributions) and the spectrum of a running laser ($A_y \neq 0$, that is with actual carrier distributions) pumped with the same current j_2. As expected, the maximum difference occurs at the laser frequency (in the running laser the electron-hole pairs are depleted, whereas in a nonlasing case they are available for transitions) and decreases for frequencies above and below ω_0.

Another representation of the spectral hole can be seen in Fig. 6(b), where we show the difference between two distribution functions, namely momentum-resolved actual electron and hole distribution functions $f^{\alpha}_{\pm i/2,\pm 1/2}$ and the corresponding Fermi-Dirac distribution functions $n^{\alpha}_{\pm i/2}$ (denoted as f_{Fermi}). The result is calculated for a laser operating in the *y*-polarized eigenmode at a pumping current $j = 2j^{thr}$. The spectral hole has its maximum at the lasing frequency, $\hbar\omega_0 - E_g - \Sigma^{thr} \approx 6.5$ meV, and is of the order of 0.1% of the value of the corresponding Fermi distribution (see inset). The spectral hole is slightly more pronounced in the k_x direction for the electric field polarized in the *y* direction because of the heavy-hole light-hole coupling in the system. This can be seen by expanding the stimulated emission term (7) for the *y*-polarized mode ($A_x = 0$) within the free carrier approximation for electron momenta close to the band edge. To second order in the wave vector, the difference in the values of stimulated emission in the two orthogonal directions in momentum space is given by

$$\left(\frac{d}{dt}\tilde{f}^{h}_{\pm 3/2,\pm 3/2}(\vec{k})\right)_s\Big|_{\vec{k}=(k,0)} - \left(\frac{d}{dt}\tilde{f}^{h}_{\pm 3/2,\pm 3/2}(\vec{k})\right)_s\Big|_{\vec{k}=(0,k)} \sim |A_y|^2\left[1-\frac{\Delta E_s}{\Delta_{hl}}\right]\frac{2\hbar\gamma_2 k^2}{m_0\Delta_{hl}}\ . \tag{21}$$

The same expressions are found for $f^{e}_{\pm 1/2,\pm 1/2}$. The asymmetry in the spectral hole resulting from the asymmetry in the stimulated emission term is therefore proportional to the light intensity and decreases with increasing hh-lh splitting. Note also that for small strain the term $\Delta E_s/\Delta_{hl}$ has only a minute influence on the shape of the spectral hole (for example, for $e_{xx} = -0.01\%$ one finds $\Delta E_s/\Delta_{hl} = 0.006$). This result is consistent with the absorption anisotropy discussed in [53–56].

V. STABILITY OF VCSEL EIGENMODES

In order to perform the stability analysis of the linearly polarized eigenmodes discussed in Sec. IV, we introduce a small, time-dependent perturbation of the eigenmode amplitudes:

$$A_x(t) = [A_x^0 + a_x(t)]e^{i\delta t}, \quad A_y(t) = [A_y^0 + a_y(t)]e^{i(\delta t+\varphi)}. \tag{22}$$

Substituting Eq. (22) into Eqs. (1)–(2) and expanding the susceptibility tensor elements $\hat{\chi}_{QW}$ around the steady-state values, one obtains the time-evolution equations for the perturbations,

$$\frac{i}{\omega_e}\frac{da_x}{dt} = \left[\frac{\delta}{\omega_e} + i\chi_B^{HE_{11''}} - \chi_0^{xx} - A_x^0\frac{\partial\chi_0^{xx}}{\partial A_x} + A_y^0\frac{\partial\chi_0^{xy}}{\partial A_x}\ e^{i\varphi}\right]a_x - \left[A_x^0\frac{\partial\chi_0^{xx}}{\partial A_x^*} - A_y^0\frac{\partial\chi_0^{xy}}{\partial A_x^*}\ e^{i\varphi}\right]a_x^* \tag{23}$$

$$+\left[\chi_0^{xy}+A_y^0\frac{\partial\chi_0^{xy}}{\partial A_y}\,e^{i\varphi}-A_x^0\frac{\partial\chi_0^{xx}}{\partial A_y}\right]e^{i\varphi}a_y$$

$$-\left[A_x^0\frac{\partial\chi_0^{xx}}{\partial A_y^*}\,e^{-i\varphi}-A_y^0\frac{\partial\chi_0^{xy}}{\partial A_y^*}\right]a_y^*,$$

$$\frac{i}{\omega_e}\frac{da_y}{dt}=\left[\chi_0^{yx}+A_x^0\frac{\partial\chi_0^{yx}}{\partial A_x}-A_y^0\frac{\partial\chi_0^{yy}}{\partial A_x}\,e^{i\varphi}\right]e^{-i\varphi}a_x$$

$$+\left[A_x^0\frac{\partial\chi_0^{yx}}{\partial A_x^*}\,e^{-i\varphi}-A_y^0\frac{\partial\chi_0^{yy}}{\partial A_x^*}\right]a_x^*+\left[\frac{\delta}{\omega_e}+i\chi_B^{HE_{11''}}\right.$$

$$\left.-\chi_0^{yy}-A_y^0\frac{\partial\chi_0^{yy}}{\partial A_y}\,e^{i\varphi}+A_x^0\frac{\partial\chi_0^{yx}}{\partial A_y}\right]a_y$$

$$+\left[A_x^0\frac{\partial\chi_0^{yx}}{\partial A_y^*}\,e^{-i\varphi}-A_y^0\frac{\partial\chi_0^{yy}}{\partial A_y^*}\right]e^{-i\varphi}a_y^*,$$

and the corresponding equations for $\dot{a}_x^*$ and $\dot{a}_y^*$. In Eqs. (23) $\omega_e=2\pi\omega_0/(1+4\pi\chi_B)$ and χ_0^{ij}, $\{i,j\}=\{x,y\}$ denote the elements of the susceptibility tensor $\hat{\chi}_{QW}$ evaluated for the eigenmode parameters $(A_x^0,A_y^0,\delta,\varphi)$. For simplicity, we do not perturb the steady-state carrier distribution functions. In other words, we consider only the class-A laser model [28], not the class-B model [24,25,27]. It has been discussed recently [31] that for small anisotropies (as in the case of unintentional strain) and short spin-flip relaxation times (a few picoseconds) the adiabatic elimination of carrier densities (i.e., the class-A model) is usually a good approximation for practical VCSELs.

The stability of polarization eigenmodes is determined by the eigenvalues λ of the matrix defined by the right-hand side (rhs) of Eqs. (23). If at least one eigenvalue has a real part larger than zero (for a given strain and pumping current) the mode is unstable. The parameter values for which the real part of the unstable eigenvalue vanishes determines the stability boundary of a given mode. We found (within a very good numerical accuracy) that for linearly polarized modes, the set of Eqs. (23) separates into two subsets, corresponding to a perturbation in the direction of the eigenmode and a perturbation in the orthogonal direction. It has been shown in Ref. [24] that the linearly polarized modes are stable with respect to perturbation in the same direction, but may be unstable for perturbations in the direction of the orthogonal mode. Our numerical solutions confirm these findings. Another interesting result obtained from the SFM model is that if the linearly polarized nonlasing mode is unstable, then the real part of the eigenvalue contributes to a broadening of its peak in the spontaneous emission spectrum, whereas the imaginary part causes a nonlinear redshift of the spontaneous emission peak [30,6,31]. The nonlinear redshift of the nonlasing mode was identified as a physical mechanism causing polarization switching. For the configuration discussed in this paper the details of the polarization switching mechanism will be presented in Sec. VI.

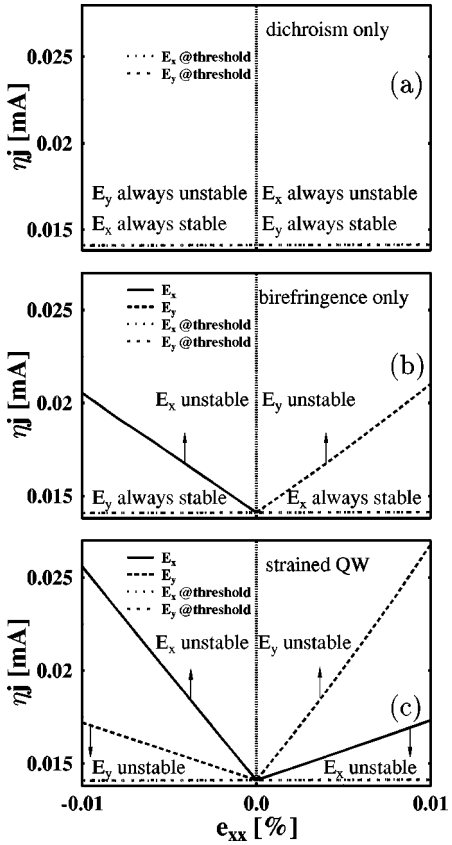

FIG. 7. Stability diagram for a microscopic class-A VCSEL model with (a) dichroism anisotropy, (b) birefringence anisotropy, and (c) the full uniaxial strain-induced anisotropy, obtained for $(\gamma_s^{e/h})^{-1}=10$ ps. The arrows indicate the regime where a given mode is unstable. Solid (dashed) curves correspond to *x*-polarized (*y*-polarized) eigenmodes. Dotted (double-dotted) curves indicate the strain-dependent threshold current for *x*-polarized (*y*-polarized) eigenmodes.

In Fig. 7 we present the stability diagram obtained for three different cases: (i) no birefringence, only gain anisotropy, (ii) no gain anisotropy, only birefringence, (iii) full calculation including both gain anisotropy and birefringence. The spin-flip time used in the calculations is $(\gamma_S^e)^{-1}=10$ ps$=(\gamma_S^h)^{-1}$. The case (i) where only the gain anisotropy but not the birefringence is included is shown in Fig. 7(a). We assume that the real parts of the susceptibility tensor depend on the strain e_{xx} as the arithmetical mean of the original values; that is, we replace the quantity $\mathrm{Re}[\chi_{QW}^{x/y,x/y}]$ by $(1/2)\mathrm{Re}[\chi_{QW}^{xx}+\chi_{QW}^{yy}]$. In this way the refractive indices for both polarizations are the same. The imaginary parts change independently, which allows for gain anisotropy. In this case the mode with larger (smaller) gain is always stable (unstable). In other words, for compressive (tensile) strain the E_x-polarized (E_y-polarized) mode experiences more gain (see Fig. 3). Therefore, for any pumping current above the threshold value, this mode is going to lase.

In Fig. 7(b) we study the case where only the birefringence is present. We proceed in a similar fashion as above, but, this time, we replace the imaginary parts $\mathrm{Im}[\chi_{QW}^{x/y,x/y}]$ by the arithmetical mean $(1/2)\mathrm{Im}[\chi_{QW}^{xx}+\chi_{QW}^{yy}]$. This causes the

gain to be polarization independent. This time, however, the real parts $\mathrm{Re}[\chi_{QW}^{x/y,x/y}]$ change independently with strain, allowing for birefringence. In this case, for compressive (tensile) strain E_y (E_x) is stable for any strain and any pumping current. However, for the orthogonal polarization the stability depends on the value of the pumping current and the strain. The arrows indicate the range of currents for which a given polarization is unstable. For instance, we see from Fig. 7(b) that, for any value of the compressive strain the laser may start lasing in any polarization and the bistable switching between two polarization states is possible. However, for pumping currents above the solid line, E_x becomes unstable and the VCSEL would lase only in *y* polarization. This type of behavior has been predicted within the phenomenological SFM description for class-A models in Ref. [27].

Next, we study in Fig. 7(c) the stability of a VCSEL with birefringence and dichroism anisotropy resulting from the uniaxial strain [case (iii)]. Here, the stability diagram is essentially a superposition of results displayed in Figs. 7(a)–7(b). For example, for any value of unintentional compressive strain the gain anisotropy determines mode stability close to threshold. Close to threshold the *x*-polarized mode is gain preferred and stable. Thus the laser starts in this polarization. However, as one increases the pumping current, the *y*-polarized mode becomes stable, which indicates that the birefringence anisotropy becomes dominant. Here, polarization switching may occur. If the pumping current is further increased, the *x*-polarized modes become unstable and the laser switches to the *y*-polarized mode, in agreement to what was observed in experiments [2–6]. Note that for tensile strain in the *x* direction, $e_{xx}>0$, one observes the same behavior but with *x* and *y* directions interchanged.

In order to study the influence of the spin-flip relaxation rate $\gamma_S^{e/h}$ on the stability boundaries, we show in Fig. 8(a) the results obtained for $(\gamma_S^{e/h})^{-1}=3$ ps, a value that was suggested by recent experiments [43]. One sees that the overall picture presented in Fig. 7(c) does not change. However, shorter spin-flip relaxation times stabilize linear polarizations, as already predicted by the SFM model [24]. Thus the polarization switching occurs at higher values of the pumping current. For instance, for a small compressive strain of $e_{xx}\approx -0.001\%$ (which might be a reasonable value for unintentional strain) our model predicts switching from *x*-(gain-preferred) to *y*-polarized (birefringence-preferred) state at $j\approx 1.5j^{thr}$, a value that is typical for experimental observations [3–5]. For comparison, we show in Fig. 8(b) the stability diagram as obtained from the free-carrier model. As one sees, the qualitative results do not change, but for a given strain the stability boundaries are shifted towards higher pumping currents. This observation might be of practical relevance, especially since it has been demonstrated that, using combined experimental measurements and theoretical fitting, one can obtain realistic estimations of spin-flip relaxation rates in practical VCSEL devices [43].

To conclude this section we note that we neglected in our considerations the influence of quantum fluctuations on the polarization dynamics and mode stability. Such studies have been performed recently for a modified SFM model in Refs. [29] and [65] (and references therein). The approach presented there allows one to obtain information about the cavity anisotropies based on the information provided by the details of the measured optical spectra. Physically, the polarization fluctuations are driven by the spontaneous emission noise. Mathematically, the spontaneous emission can be incorporated into the analysis by adding Langevin noise sources to the right-hand side of the equations for the perturbation amplitudes (23). The solution of this type of equations leads to optical spectra of VCSELs and has been previously obtained for the SFM model by spectral decomposition (as in Ref. [65]) and via Green functions (see Ref. [29]) approaches. Note that in the latter approach one explicitly uses the eigenvalues λ, which determine the stability diagram of anisotropic VCSELs. The addition of spontaneous emission does not modify the polarization stability of eigenmodes. It allows, however, for a quantitative estimation of how stable the lasing mode is and how much the polarization fluctuates around its steady-state value. However, these problems are beyond the scope of the research presented in this paper and therefore we restrict ourselves only to the discussion of polarization stability diagrams and neglect the details of the polarization fluctuations (i.e., spontaneous emission noise).

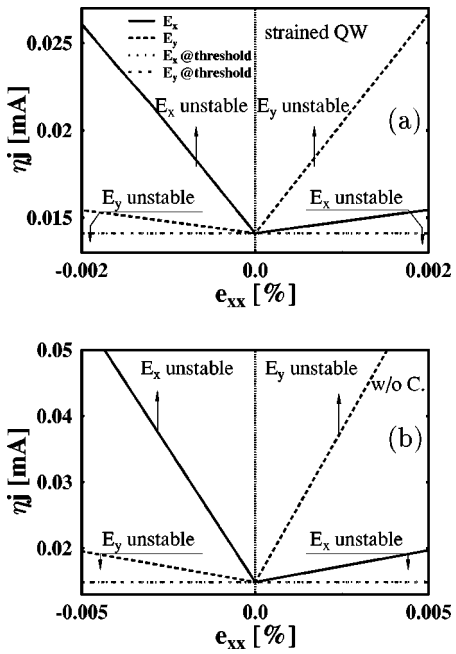

FIG. 8. Same as in Fig. 7(c), but for $(\gamma_s^{e/h})^{-1}=3$ ps. The results were obtained using the (a) many-body and (b) free-carrier models.

VI. PHYSICAL INTERPRETATION OF POLARIZATION SWITCHING

In this section we discuss the possible mechanism leading to destabilization of the output polarization. As an example, we consider the structure with compressive uniaxial strain $e_{xx}=-0.0015\%$, and $(\gamma_S^{e/h})^{-1}=3$ ps. We study the conditions under which the gain-preferred *x* polarization becomes unstable and the laser switches to the birefringence preferred (stable) *y* polarization as the pumping current increases.

The physical explanation, within the SFM model, in terms of pumping-current-induced nonlinear anisotropy and the resulting frequency shift was given in Refs. [31,6]. It has been shown that in the case of dominant birefringence (two orders of magnitude larger than the gain anisotropy) and large linewidth enhancement factor, the switching from the low-frequency to the high-frequency mode [see Fig. 2(b) in Ref. [31]] occurs as the result of decreasing frequency splitting between lasing and nonlasing mode. For example, for the lasing *x*-polarized (low-frequency) mode the modal frequencies are given by

$$\omega_x = -\omega_0 + \delta_x, \quad \omega_y = -\omega_0 + \omega_e \,\mathrm{Re}[\chi_{QW}^{yy}] + \mathrm{Im}[\lambda], \tag{24}$$

where δ_x is given by δ in Eq. (18) and $\mathrm{Im}[\lambda]$ represents the nonlinear anisotropy contribution. Similarly, for the lasing *y*-polarized (high-frequency) mode we have

$$\omega_y = -\omega_0 + \delta_y, \quad \omega_x = -\omega_0 + \omega_e \,\mathrm{Re}[\chi_{QW}^{xx}] + \mathrm{Im}[\lambda], \tag{25}$$

where δ_y is given by Eq. (19). For the case considered here (switching from *x* polarization to *y* polarization) the change of the frequency splitting was caused by the nonlinear anisotropies, which are mathematically represented by the imaginary part of the complex eigenvalues λ in Eq. (24). However, the switching scenario reported in Ref. [31] does not apply to the case discussed in this paper. To demonstrate this, we show in Fig. 9(a) how the complex eigenvalues change with increasing current. Strictly speaking, for each polarization, there are two complex conjugate eigenvalues (for low current), which become real for the currents indicated by kinks on the $\mathrm{Re}[\lambda]$ curves. For each polarization only one eigenvalue is shown in Fig. 9(a). At the switching point (the real part of the eigenvalue λ, shown as a solid line, becomes positive, see the point indicated by an arrow) the imaginary parts of eigenvalue (dotted line) is zero. That contradicts the mechanism causing destabilization of *x* polarization reported in Ref. [31]. The discrepancy is due to the fact that in our case the birefringence and the gain anisotropy are of the same order of magnitude whereas in Ref. [31] they differ by two orders of magnitude. Indeed, we performed numerical simulations of Eq. (16) in Ref. [31], but for the set of parameters corresponding to this paper, and we found similar behavior to that shown in Fig. 9(a).

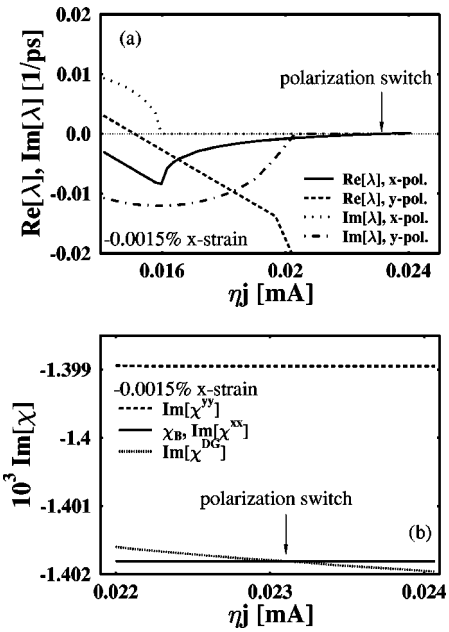

FIG. 9. (a) Complex eigenvalues of the stability analysis for *x*- and *y*-polarized lasing modes as a function of the pumping current. Only one dominant eigenvalue is shown for each polarization. (b) Cavity loss and modal gain for the lasing *x*-polarized mode (solid line), modal gain for the nonlasing *y*-polarized mode (dashed line), and the differential off-diagonal gain (dots) for the elliptical mode in the vicinity of the switching point as a function of pumping current. The arrow indicates the pumping current for which the polarization switching occurs.

In order to find a possible mechanism responsible for the destabilization of the gain-preferred *x*-polarized mode for the strain induced anisotropy considered in this paper, we examine the linear stability equations for perturbation amplitudes (23) in the vicinity of $\lambda = 0$. As mentioned before, within a good numerical accuracy this set of equations splits into two separate subsets of equations, one for (a_x, a_x^*) and another one for (a_y, a_y^*). For the *x*-polarized lasing mode, we consider the equations for perturbation amplitudes in the orthogonal direction of polarization (that is, for a_y and a_y^*), as the eigenvalue for these amplitudes acquires a positive real part and destabilizes the lasing mode.

An approximate expression for the eigenvalue λ in the vicinity of the switching point, $|\lambda| \ll 1$, is given by

$$\lambda \approx \frac{|(\delta_x/\omega_e) + i\chi_B^{HE''_{11}} - \chi_0^{yy} + A_x^0(\partial\chi_0^{yx}/\partial A_y)|^2 - |A_x^0(\partial\chi_0^{yx}/\partial A_y^*)|^2}{\chi_B^{HE''_{11}} - \mathrm{Im}[\chi_0^{yy} - A_x^0(\partial\chi_0^{yx}/\partial A_y)]}, \tag{26}$$

and the right eigenvector associated with this eigenvalue is

$$\begin{pmatrix} a_{1y}^{(r)} \\ a_{1y}^{(i)} \end{pmatrix} = \begin{pmatrix} (\delta_x/\omega_e) - \mathrm{Re}[\chi_0^{yy} - A_x^0(\partial\chi_0^{yx}/\partial A_y) + A_x^0(\partial\chi_0^{yx}/\partial A_y^*)] \\ (\lambda/\omega_e) - \chi_B^{HE''_{11}} + \mathrm{Im}[\chi_0^{yy} - A_x^0(\partial\chi_0^{yx}/\partial A_y) - A_x^0(\partial\chi_0^{yx}/\partial A_y^*)] \end{pmatrix}, \tag{27}$$

where $a_{1y}^{(r)}$ and $a_{1y}^{(i)}$ denote the real and imaginary components of the eigenvector, respectively. In deriving Eqs. (26)–(27) we used the fact that Eq. (23) does not depend on the phase φ (for the equations considered here), therefore we put $\varphi=0$.

In the complex plane, the direction of the eigenvector (27) defines the direction in which the perturbation destabilizing the lasing mode is going to grow. From the numerical calculations we found that at the switching point the phase of the eigenvector (27) is

$$\varphi_\lambda = \mathrm{Arg}[a_y] \approx -0.1\pi, \tag{28}$$

and changes from about -0.09π to -0.11π for the range of pumping currents shown in Fig. 9(b). The time-evolution equation (23) for the magnitude of the perturbation amplitude a_y (27) can be written in the form

$$\frac{d|a_y|}{dt} = (\chi_B^{HE''_{11}} - \chi^{DG})|a_y|, \tag{29}$$

$$\chi^{DG} = \mathrm{Im}\left[\chi_0^{yy} - A_x^0 \frac{\partial \chi_0^{yx}}{\partial A_y}\right] - A_x^0 \left|\frac{\partial \chi_0^{yx}}{\partial A_y^*}\right| \cos(\varphi_\lambda - \varphi_\chi),$$

where $\varphi_\chi = 1/2\,\mathrm{Arg}[(\partial \chi_0^{yx}/\partial A_y^*)]$ and the phase φ_λ is given by the phase of the eigenvector (27).

The steady-state condition for Eq. (29), $\chi_B^{HE_{11}''} = \chi^{DG}$, resembles the steady-state gain-equal-loss condition for linearly polarized modes. However, in the present case χ^{DG} corresponds rather to differential off-diagonal gain (superscript ''DG'') of the medium driven by the small perturbations in the direction given by the eigenvector (27). Note, that χ^{DG} contains contributions from both diagonal and off-diagonal elements of the susceptibility tensor $\hat{\chi}_{QW}$. A superposition of the lasing mode amplitude with the phase-shifted small perturbation leads to a very elongated elliptically polarized state. If the differential off-diagonal gain seen by the perturbation is smaller (larger) than the cavity loss, the laser stays in (switches from) the original linear polarization state (to the orthogonal state). In other words, the transition from one polarization to another is accompanied by the creation of the elliptically polarized state, and the lasing mode becomes unstable if the gain seen by the perturbation amplitude is larger than the cavity loss, so such a state can be supported by the cavity as a lasing mode. To support this conjecture, we show in Fig. 9(b) the differential off-diagonal gain $\mathrm{Im}[\chi^{DG}]$ (dotted line) as a function of a pumping current. One sees that $\mathrm{Im}[\chi^{DG}]$ crosses the value of the cavity loss (shown as a solid line) at the switching current, and becomes larger than $\chi_B^{HE''_{11}}$ for larger currents. For comparison, the gain corresponding to the nonlasing *y* polarization is shown as a dashed line. Note also that the presented mechanism is consistent with the explanation of the role played by elliptical polarization in the polarization switching process described in Sec. III C of Ref. [31].

VII. SUMMARY

In summary, we have derived a microscopic model for VCSELs that is based on a rigorous solution of Maxwell's equations coupled to generalized semiconductor Bloch equations. This allows for a realistic modeling of optically anisotropic lasers. The optical part of the model includes a detailed characterization of VCSEL structures (thicknesses, radial sizes, and refractive indices of cavity layers) and is based on a self-consistent solution of the cold-cavity 3D vectorial eigenmodes. The vectorial eigenmodes are then coupled to the electronic part of the model, which is based on a microscopic theory for the optical response of semiconductor quantum wells describing potentially anisotropic valence bands, and the dynamics of charge carriers and of the interband polarizations including Coulomb interaction. The theory is evaluated in a simplified version containing approximations such as the adiabatic elimination of polarizations and the relaxation-rate approximation. We discussed in detail the steady-state vector-polarization eigenmodes of VCSELs and their linear stability properties within the two-mode, four-band, class-A model approximations. We investigated the role of Coulomb terms in the steady-state IO characteristics.

Our investigation of the influence of anisotropic strain of the optically active quantum well is based on the hypothesis that this is the dominant source of experimentally observed VCSEL characteristics. However, this theory can also be applied to recently designed uniaxially strained VCSELs [15]. For small uniaxial strain (less than 0.01%) the input-output characteristics of linearly polarized eigenmodes are not significantly modified. However, the stability properties of these modes depend strongly on the sign and the value of the anisotropy. We found that the relative ratio of birefringence to anisotropy depends on the carrier density, and therefore on factors like cavity quality and tuning. The stability analysis predicts that, if a small anisotropic strain is present, the laser will start operating in the polarization, which is gain preferred. However, if one increases the pumping current, the orthogonal polarization becomes stable. As a result of internal fluctuations, polarization switching and/or self-oscillations may occur. For even higher pumping currents, the initial polarization becomes unstable and laser switches to the birefringence-preferred eigenstate. It should be pointed out that the scenario presented here has also been predicted by the phenomenological SFM model for various configurations of model parameters [24,25,27,31]. The advantage of the model presented here is that it provides a first-principles calculation of intentional [15] or unintentional anisotropies that can occur in practical devices. Further developments of our theory are possible by considering the details of anisotropic carrier-carrier and carrier-phonon scattering, as well as taking into account temperature effects and higher-order transverse mode competition effects through spatial-spectral hole burning.

ACKNOWLEDGMENTS

We would like to thank Thomas Rössler of the Arizona Center for Mathematical Sciences, University of Arizona;

Michael Wraback of the Army Research Laboratories; and Ewan Wright of the Optical Sciences Center, University of Arizona, for helpful discussions. Financial support for this work has been provided by the Joint Services Optics Program (JSOP), the Army Research Office (ARO), COEDIP (University of Arizona), and the Air Force Office of Scientific Research (AFOSR).

APPENDIX A: THE OPTICAL MODEL OF VCSELS

In this Appendix we derive directly from Maxwell's equations the rate equation for the slowly varying amplitudes of vectorial eigenmodes of index-guided VCSELs [47,48]. The Maxwell's equations (in Gaussian units) inside the quantum-well layer can be written in the form

$$\vec{\nabla}\times\vec{\nabla}\times\vec{E}=-\frac{1}{c^2}\frac{\partial^2\vec{D}}{\partial^2 t}\ , \tag{A1}$$

where $\vec{E}$ denotes the vector of an electric field, c is the speed of light in vacuum, and the relationship between the displacement $\vec{D}$ and electric field $\vec{E}$ vectors is given by

$$\vec{D}=\vec{E}+4\pi\vec{P}_B+4\pi\vec{P}_{QW}, \tag{A2}$$

with $\vec{P}_B$ and $\vec{P}_{QW}$ being the background and active quantum well polarization vectors, respectively. The material polarization vectors $\vec{P}_B$ and $\vec{P}_{QW}$ are related to the electric field via the material susceptibility tensors $\hat{\chi}_B$ and $\hat{\chi}_{QW}$, respectively.

$$\vec{P}_{QW}^{(-)}(t)=\int_{-\infty}^{t}\hat{\chi}_{QW}(t-\tau)\cdot\vec{E}^{(-)}(\tau)d\tau, \tag{A3}$$

where the superscript ''$-$'' indicates the negative-frequency contribution. We will assume that the time response of background susceptibility tensor $\hat{\chi}_B$ is infinitely fast and any memory effects can be neglected, therefore $\vec{P}_B^{(-)}(t)=\hat{\chi}_B\cdot\vec{E}^{(-)}(t)$.

1. Cold-cavity vectorial eigenmodes

In this section we extend the theory of cold-cavity vectorial eigenmodes of VCSELs [47,48] to make it applicable for the analysis of running lasers. We choose the dominant time dependence to be $e^{-i\omega t}$, so the forward/backward ($\mp$ sign in front of the longitudinal propagation constant) propagating fields in Ref. [47] correspond to backward/forward ($\mp$ sign at the longitudinal propagation constant) propagating fields in this paper. In the calculation of cold-cavity vectorial eigenmodes one neglects the influence of the QW, that is $\vec{P}_{QW}=0$. For isotropic cavities the susceptibility tensor $\hat{\chi}_B$ can be characterized by one scalar number, which in general can be complex. One can factor the electric field vector into time and space depending parts, that is

$$\vec{E}_\mu(\vec{r},t)=\frac{1}{2}\vec{E}_\mu^{(s)}(\vec{r})e^{-i\omega_\mu t}+\text{c.c.}, \tag{A4}$$

where $\mu=(n,l)$ is a mode index of the cold-cavity hybrid mode determined by azimuthal n and radial l mode orders (see Ref. [47]), ω_μ is the mode frequency, and c.c. indicates complex conjugate. Thus, the Maxwell equations for the eigenmode μ can be written as

$$\vec{\nabla}\times\vec{\nabla}\times\vec{E}_\mu^{(s)}(\vec{r})-\frac{\omega_\mu^2}{c^2}\ (1+4\pi\chi_B^\mu)\vec{E}_\mu^{(s)}(\vec{r})=0. \tag{A5}$$

Note that the solution of Eq. (A5) describes the 3D electric field with (in general) three nonvanishing vector components at the location of the quantum well. In order to calculate the electric field outside the QW region one can use the vectorial transform matrix method described in Ref. [47]. Within that formulation the amplitudes of the forward ($\vec{A}_0^-$) and backward ($\vec{A}_0^+$) propagating fields at the front plane are related to the amplitudes of forward ($\vec{A}_{N+1}^-$) and backward ($\vec{A}_{N+1}^+$) propagating fields at the rear plane via the vectorial transform matrix

$$\begin{pmatrix}\vec{A}_{N+1}^-\\ \vec{A}_{N+1}^+\end{pmatrix}=\begin{pmatrix}M^{--} & M^{-+}\\ M^{+-} & M^{++}\end{pmatrix}\begin{pmatrix}\vec{A}_0^-\\ \vec{A}_0^+\end{pmatrix}, \tag{A6}$$

where the elements of matrices $M^{\pm\pm}$ are described in detail in Ref. [47], N is the number of interfaces in the structure in the longitudinal direction, and $\vec{A}_l^{\pm}$ is a vector with elements being the amplitudes of modes that are used for field decomposition. The lasing condition is that only the outgoing amplitudes from the VCSEL are nonzero, which transforms Eq. (A6) to the form

$$M^{--}\vec{A}_0^-=0, \quad \vec{A}_{N+1}^+=M^{+-}\vec{A}_0^-. \tag{A7}$$

By evaluating the total vectorial matrix M at appropriate planes, one can express the amplitudes $\vec{A}_{N+1}^+$ and $\vec{A}_0^-$ in terms of amplitudes in the active layer (denoted by layer number l_A). Denoting the elements of the vectorial transform matrix between the front plane and the active layer by $M_{l_A}^{\pm\pm}$, one finds from the first condition of Eq. (A7)

$$\vec{A}_{l_A}^-=M_{l_A}^{--}\vec{A}_0^-, \quad \vec{A}_{l_A}^+=M_{l_A}^{+-}(M_{l_A}^{--})^{-1}\vec{A}_{l_A}^-. \tag{A8}$$

There is only one independent, undetermined component of the vector $\vec{A}$, or, in other words, mode amplitude, which characterizes a given cold-cavity eigenmode. In this paper, we identify the forward propagating amplitude coefficient in the active layer to be the (undetermined, as for now) mode amplitude. All other amplitudes can then be found from Eq. (A8) and from transform matrices for other layers.

The hybrid modes of semiconductor layers in VCSELs that are characterized by different azimuthal mode numbers are orthogonal to each other [66]. Thus the spatial profile of the electric field of any VCSEL eigenmode $\vec{E}_{nl}^{(s)}(\vec{r})$ in any layer (and, in particular, in the active one) is given as a superposition over only the radial mode numbers. The spatial

profiles used for a superposition are given by the transverse profiles of optical fibers hybrid (bound and radiation) modes $\vec{E}^{F\pm}_{n\kappa}$ [47]

$$\vec{E}^{(s)}_{nl}(\vec{r}) = \sum_{\kappa} (\vec{E}^{F+}_{n\kappa} + \vec{E}^{F-}_{n\kappa}) = A^{-}_{nl} \sum_{\kappa} (a^{+}_{n\kappa} e^{i\gamma^{n\kappa} z} - a^{-}_{n\kappa} e^{-i\gamma^{n\kappa} z}) \vec{e}^{F}_{n\kappa}(\vec{r}), \quad \text{(A9)}$$

where $\gamma^{n\kappa}$ is the longitudinal propagation constant of a given fiber mode, $a^{-}_{nl}=1$ and the remaining amplitude coefficients are determined by Eq. (A8). The spatial dependence of $\vec{e}^{F}_{n\kappa}(\vec{r})$ is specified explicitly in Tables I and II of Ref. [47]. For index-guided VCSELs the transverse profile of eigenmode (n,l) resembles very well the corresponding profile of the (n,l) hybrid mode of optical fiber. This means that one can identify the radial mode order l by determining the largest amplitude coefficient, that is $|a^{-}_{n\kappa}| \ll |a^{-}_{nl}|$ for $\kappa = 1,2,\ldots,\kappa \neq l$. For air-post index-guided cavities considered in this paper one can (within very good accuracy) limit the expansion to only a small number N^{max} of bound modes (as a matter of fact, for cavities considered here the dominant amplitude coefficient is four orders of magnitude larger than the remaining ones; therefore we use $N^{max}=10$ bound modes).

Each VCSEL eigenmode $\mu=(n,l)$ is characterized by two parameters: the eigenfrequency ω_μ and the imaginary part of the complex susceptibility, $\chi^{\mu}_{B} = \chi^{\mu'}_{B} + i\chi^{\mu''}_{B}$, describing the modal cavity loss. These parameters have to be found from the condition of nonzero amplitude solutions in Eq. (A7), $\det[M^{--}(k^{\mu}_{A})]=0$, with k^{μ}_{A} being the complex wave number of the eigenmode μ in the active layer. They are related to the set of transverse ($\beta^{n\kappa}$) and longitudinal ($\gamma^{n\kappa}$) propagation constants via the relation

$$k^{nl}_{A} = \sqrt{(\beta^{n\kappa})^2 + (\gamma^{n\kappa})^2}, \quad \text{(A10)}$$

for each $\kappa=1,2,\ldots,N^{max}$ in the eigenmode expansion, and to the complex background susceptibility χ^{μ}_{B} via

$$(k^{\mu}_{A})^2 = 1 + 4\pi\chi^{\mu}_{B}, \quad \text{(A11)}$$

where $k^{\mu}_{A} = (2\pi/\lambda^{\mu}_{R}) n_A + i k^{\mu''}_{A}$, $\gamma^{n\kappa} = (2\pi/\lambda^{\mu}_{R}) n_{eff} + i\gamma^{n\kappa''}$, with $\gamma^{n\kappa''}$ and $k^{\mu''}_{A}$ denoting the imaginary part of $\gamma^{n\kappa}$ and k^{μ}_{A}, respectively, $\lambda^{\mu}_{R} = \omega_\mu / c$ being the resonant wavelength of mode μ, and n_{eff} being the effective refractive index with respect to the longitudinal propagation direction. Similarly as in Ref. [48], we consider only high-quality cavities, and so the modes of lossless optical fibers are used as a basis underlying our numerical solutions. This leads to the real values of transverse propagation constants $\beta^{n\kappa}$. Numerical solution of the condition $\det[M^{--}(k^{\mu}_{A})]=0$ leads to the values of λ^{μ}_{R} and $k^{\mu''}_{A}$, which, together with Eqs. (A10) and (A11) are used to calculate ω_μ, $\chi^{\mu''}_{B}$ and γ^{μ}, the parameters that are used in the mode expansion procedure. Another important parameter is the effective dimensionless cavity loss $\gamma^{nl''} L_{cav}$, where L_{cav} is the cavity length. In the single lasing mode case, the steady state can be achieved when the modal loss $\gamma^{nl''} L_{cav}$ is compensated by a modal gain $\alpha^{\mu} L_{QW}$ from a quantum well, i.e., when $\gamma^{nl''} L_{cav} = \alpha^{\mu} L_{QW}$.

2. Field amplitudes in running VCSELs

In order to analyze the field evolution in the running laser, let us consider first the time evolution of the microscopic quantum well polarization vector $\vec{P}_{QW}$. Transforming Eq. (A3) into the frequency space, one obtains

$$\vec{P}^{(-)}_{QW}(\vec{r},\omega) = \hat{\chi}_{QW}(\omega) \cdot \vec{E}^{(-)}(\vec{r},\omega) \approx \left[\hat{\chi}_{QW}(\omega_0) + (\omega-\omega_0) \frac{\partial \hat{\chi}_{QW}}{\partial \omega} \bigg|_{\omega=\omega_0} + \cdots \right] \cdot \vec{E}^{(-)}(\vec{r},\omega), \quad \text{(A12)}$$

where the Taylor expansion of the frequency dependent susceptibility tensor $\hat{\chi}_{QW}(\omega)$ has been performed around a reference frequency ω_0 that will be specified later. Neglecting all the terms involving derivatives with respect to frequency and Fourier transforming back into time one obtains

$$\vec{P}^{(-)}_{QW}(\vec{r},t) = \hat{\chi}_{QW}(\omega_0) \cdot \vec{E}^{(-)}(\vec{r},t). \quad \text{(A13)}$$

This approximation is valid if one considers the properties of steady-state laser eigenmodes, where the dominant time dependence is determined by the laser frequency ω_0.

Next, we perform the decomposition of the electric field into the cold-cavity eigenmodes with slowly varying amplitudes

$$\vec{E}(\vec{r},t) = \frac{1}{2} e^{-i\omega_0 t} \sum_{\mu} \vec{E}^{(s)}_{\mu}(\vec{r},t) e^{-i(\omega_\mu - \omega_0)t} + \text{c.c.}, \quad \text{(A14)}$$

where the superscript (s) has a similar meaning as in Eq. (A4); however, we now allow for a slow time dependence of the fields. According to Eq. (A13), one can write the QW polarization in a similar way:

$$\vec{P}_{QW}(\vec{r},t) = \frac{1}{2} \vec{P}^{(s)}_{QW}(\vec{r},t) e^{-i\omega_0 t} + \text{c.c.} \quad \text{(A15)}$$

Substituting Eqs. (A15) and (A14) into Maxwell's equations (A1), neglecting first and second time derivatives of the polarization and second time derivatives of the electric field (slowly varying amplitude approximation), neglecting terms with fast harmonic time variation (rotating wave approximation), using the cavity eigenmode equation (A5) and neglecting the dispersion of the background susceptibility, one obtains the time evolution equation for the electric field vector in the quantum well layer

$$\sum_{\mu} e^{-i(\omega_\mu-\omega_0)t}\Big[-2\pi\omega_\mu^2\chi_B^{\mu''}\vec{E}_\mu^{(s)}(\vec{r},t) + \omega_\mu(1+4\pi\chi_B)\frac{\partial}{\partial t}\vec{E}_\mu^{(s)}(\vec{r},t)\Big] = 2i\pi\omega_0^2\vec{P}_{QW}^{(s)}(\vec{r},t). \tag{A16}$$

In order to find the time evolution equation for each mode separately, one should consider a total field that is a superposition of forward and backward running fields. However, since these two fields are orthogonal to each other and since they are related via Eq. (A8), it is sufficient to consider only backward propagating modes in the expansion (A9)

$$\vec{E}_{nl}^{(s)}(\vec{r}) = A_{nl}^{-}(t)\sum_{\kappa=1}^{N^{max}} a_{n\kappa}^{-}\vec{e}_{n\kappa}^{F}(\vec{r})e^{i\gamma^{n\kappa}z}, \tag{A17}$$

where the amplitude $A_\mu^-(t)$ is slowly changing in time. As mentioned earlier, the resonance condition (A7) for the cavity eigenmode allows us to determine uniquely the amplitudes of the electric field in all other layers in the cavity. In the following we assume that it is sufficient to expand the electric field only in terms of eigenmodes with different azimuthal number and different polarizations, but with the same radial mode number. This assumption is justified by the observation that neighboring higher-order azimuthal modes are spectrally closer to the fundamental mode and have smaller modal losses than the higher-order radial modes, and therefore are gain preferred. Applying the orthogonality condition for hybrid modes of optical fibers [66], using Eq. (A13), and averaging over the thickness of the quantum well (which is about three orders of magnitude smaller than a typical wavelength and carrier diffusion length), one obtains a set of evolution equations describing the modal dynamics of light inside the VCSEL:

$$e^{-i(\omega_\mu-\omega_0)t}\Big[-2\pi\omega_\mu^2\chi_B^{\mu''}A_\mu^-(t)+\omega_\mu(1+4\pi\chi_B)\frac{\partial A_\mu^-(t)}{\partial t}\Big] \times\sum_{\kappa=1}^{N^{max}}(N_{n\kappa}a_{n\kappa}^-)^2 = 2i\pi\omega_0^2\sum_{n'}\sum_{\kappa'=1}^{N^{max}}\sum_{\kappa=1}^{N^{max}}A_\nu^-(t)a_{n\kappa}^-a_{n'\kappa'}^- \times e^{-i(\omega_\nu-\omega_0)t}\int\int_{\mathcal{A}}\{[\hat{\chi}_{QW}\cdot\vec{e}_\nu(r,\varphi)]\vec{h}_\mu(r,\varphi)\}\cdot\hat{z}d\mathcal{A}. \tag{A18}$$

This holds for each hybrid eigenmode μ taken into the field expansion, and the abbreviated notation $\mu=(n,l)$ and $\nu=(n',l')$ has been used. In Eq. (A18), $\mathcal{A}$ is the cross section of the device, $N_\mu^2=\int_{\mathcal{A}}[\vec{e}_\mu(r,\varphi)\vec{h}_\mu(r,\varphi)]\cdot\hat{z}d\mathcal{A}$ defines the normalization factor of the mode, $\vec{h}_\mu(r,\varphi)$ describes the spatial variation of the magnetic field in the QW layer, and $\hat{z}$ is the unit vector perpendicular to the surface of the QW.

Equation (A18) is the central equation of the optical part of the model. It describes mode coupling via spatial hole burning, since the susceptibility tensor $\hat{\chi}_{QW}$ can be a nonuniform function in the transverse direction due to existing fields as well as can be anisotropic because of some intentional or unintentional strain in the lattice structure. Thus the overlap integral on the rhs of Eq. (A18) depends explicitly on (i) the overlap of the gain profile with the modal electric field profile, and (ii) the change of the electric field direction and amplitude and the resulting change of overlap with magnetic fields of other modes.

3. Two-mode laser model

In order to study polarization switching phenomena close to threshold, we evaluate Eqs. (A18) for the case of two (mutually orthogonal) transverse HE_{11}-like modes. The model will be applicable to small-area cavities, or, equivalently, to larger cavities where fundamental-mode lasing has been achieved, for instance, by modifying the cavity structure (oxidization, introduction of antiguiding sections, etc.). We choose the reference frequency ω_0 to be the frequency of the two degenerate hybrid modes: $\omega_0=\omega_{HE_{11}}$. Numerical solutions for cold-cavity eigenmodes show that the dominant radial mode amplitude coefficient $a_{nl}^{\pm}$ in the expansion (A9) is several orders of magnitude larger than the remaining coefficients $a_{n\kappa}^{\pm}$. It is therefore a very good approximation to consider only the fundamental radial (1,1) mode in the analytical considerations that follow.

The Cartesian components of the HE_{11} modal electric fields are given by

$$e_x^\mu=e_r^\mu\cos\varphi-e_\varphi^\mu\sin\varphi,\quad e_y^\mu=e_r^\mu\sin\varphi+e_\varphi^\mu\cos\varphi, \tag{A19}$$

where $\mu=1,2$ is the mode number, and the spatial variation of modal fields *inside* the core of the laser (we neglect the field outside) is given by (see Table I in Ref. [47])

$$e_r^{(1)}=-\left(\frac{k_0}{\gamma}\frac{n}{r}\,J_1(\beta r)+B\frac{\gamma}{k_0}\,J_1'(\beta r)\right)\cos\varphi\equiv-f_1(r)\cos\varphi, \tag{A20}$$

$$e_\varphi^{(1)}=-\left(\frac{k_0}{\gamma}\,J_1'(\beta r)+B\frac{\gamma}{k_0}\frac{m}{r}\,J_1(\beta r)\right)\sin\varphi\equiv-f_2(r)\sin\varphi.$$

In Eq. (A20) J_1 denotes the first-order Bessel function ($n=1$ is the azimuthal mode order), k_0 is the wave number in the free space, B is the relative amplitude of the TM_z to TE_z contributions to the hybrid mode [given by Eq. (7a) in Ref. [47]], and β is the transverse propagation constant entering Eqs. (A10)–(A11). As for the fundamental mode, one can assume (within very good numerical accuracy) that $f_1(r)=f_2(r)=f(r)$. Thus, one can find from Eq. (A19) $\vec{e}^{(1)}=[0,-f(r),e_z^{(1)}]$. Another cold-cavity solution of Maxwell equations in the QW layer can be obtained from Eq. (A20) upon the substitution $\cos\varphi\to\sin\varphi$, $\sin\varphi\to-\cos\varphi$, which leads to the orthogonally polarized mode $\vec{e}^{(2)}=[f(r),0,e_z^{(2)}]$. Note that rigorous modal solutions for VC-

SEL eigenmodes are not described by Gaussian functions, as it is usually assumed, but by superpositions of Bessel functions. Similarly, for magnetic fields, one obtains $\vec{h}^{(1)}=[-g(r),0,h_z^{(1)}]$, and $\vec{h}^{(2)}=[0,g(r),h_z^{(2)}]$, where $J_1'(\beta r)+Bn_A^2(n/r)J_1(\beta r)=g(r)=(n/r)J_1(\beta r)+Bn_A^2J_1'(\beta r)$. In the following we will neglect the z components of the electric and magnetic fields, $e_z^{(\mu)}$ and $h_z^{(\mu)}$, as they are usually two orders of magnitude smaller than the dominant components in the transverse direction. However, this approximation is valid for the fundamental and first few higher-order azimuthal modes only, because the magnitude of these components increases with the square of the transverse propagation constant, β^2, and β changes from $\beta^{fund}\approx 0$ (fundamental mode) to $\beta^{cutoff}\approx n_A k_0$ for a mode at cutoff (highest radial order transverse mode confined to the structure). Thus we reduce the 3×3 susceptibility tensor $\hat{\chi}_{QW}$ to 2×2 matrix.

The set of fundamental modes considered in our analysis is therefore given by

$$\begin{aligned}
&\vec{e}^{(1)}=(0,-f(r),0), \quad \vec{h}^{(1)}=(-g(r),0,0),\\
&\vec{e}^{(2)}=(f(r),0,0), \quad \vec{h}^{(2)}=(0,-g(r),0),\\
&\vec{e}^{(tot)}=A_y^-(t)\vec{e}^{(1)}+A_x^-(t)\vec{e}^{(2)},\\
&\vec{h}^{(tot)}=A_y^-(t)\vec{h}^{(1)}+A_x^-(t)\vec{h}^{(2)},
\end{aligned} \tag{A21}$$

where $\vec{e}^{(tot)}$ and $\vec{h}^{(tot)}$ denote the vectors of the total electric and magnetic fields entering the microscopic material equations that will be derived in the next section. We introduced the mode amplitudes according to $A_{y/x}^-=A_{1/2}^-$. As for the fundamental modes of the same transverse profiles, the effects of mode competition due to spatial hole burning are negligible and one can use a susceptibility tensor $\hat{\chi}_{QW}$ that is averaged over the transverse direction. Under this assumption Eq. (A18) can be rewritten in the form given by Eqs. (1)–(2), where we introduced the amplitudes of the *total* electric field $A_{x/y}=A_{x/y}^-(1+a_{11}^+)$ [$|a_{11}^+|\approx 0.992$ is the numerical value for the amplitude coefficient of the forward propagating field obtained from a numerical solution of Eqs. (A7)–(A8) for the cavity under consideration].

APPENDIX B: ELECTRONIC MODEL OF UNIAXIALLY STRAINED QUANTUM WELLS

In this appendix we derive a simplified expression for a quantum-well susceptibility tensor $\hat{\chi}_{QW}$, including possible anisotropic strain effects. To simplify the model, we consider only high-Q cavities so that the amount of carriers necessary to provide lasing is not too large. This allows us to neglect the light-hole contribution to the gain, since the heavy-hole light-hole splitting is larger than, or of the order of, the gain bandwidth. Our model incorporates the uniaxial strain effects on the QW gain and refractive index according to Refs. [52–56], with many-body generalizations according to Refs. [57–59].

1. Semiconductor Bloch equations for a six-band model

The semiconductor Bloch equations (SBEs) describing optical transitions in a QW are the equations of motion for the time-dependent optical polarization functions $P_{sj}(\vec{k})$ as well as the electron and hole distribution/coherence functions $f_{ss'}(\vec{k})$ and $f_{jj'}(\vec{k})$, respectively. The vector $\vec{k}$ is the two-dimensional in-plane wave vector, the electron quantum numbers s, s' denote the spin-degenerate conduction bands with $s=\pm 1/2$, and the hole quantum numbers j, j' denote the two degenerate heavy-hole ($j=\pm 3/2$) and light-hole ($j=\pm 1/2$) bands. The various terms entering the equations below have been introduced and explained in Sec. II B. The coherent contributions to these equations are [59] (scattering and electrical pumping terms will be added later)

$$\begin{aligned}
i\hbar\frac{d}{dt}P_{sj}(\vec{k})=&\sum_{s'j'}\{[\delta_{ss'}\delta_{jj'}\varepsilon_k^s+\delta_{ss'}\mathcal{H}_{jj'}(-\vec{k})]P_{s'j'}(\vec{k})\\
&-\Omega_{s'j'}^{(ren)}(\vec{k})[\delta_{ss'}\delta_{jj'}-\delta_{jj'}f_{ss'}(\vec{k})\\
&-\delta_{ss'}f_{jj'}(\vec{k})]+[\delta_{jj'}\Sigma_{ss'}(\vec{k})\\
&+\delta_{ss'}\Sigma_{jj'}(-\vec{k})]P_{s'j'}(\vec{k})\}-i(1/T_2)P_{sj}(\vec{k}),
\end{aligned} \tag{B1}$$

$$\begin{aligned}
i\hbar\frac{d}{dt}f_{jj'}(\vec{k})=&\sum_{j''}\mathcal{H}_{jj''}(\vec{k})f_{j''j'}(\vec{k})-f_{jj''}(\vec{k})\mathcal{H}_{j''j'}(\vec{k})\\
&+\sum_s\{(\Omega^{(ren)})_{sj'}^*(-\vec{k})P_{sj}(-\vec{k})\\
&-\Omega_{sj}^{(ren)}(-\vec{k})P_{sj'}^*(-\vec{k})\}\\
&+\sum_{j''}\{\Sigma_{jj''}(\vec{k})f_{j''j'}(\vec{k})-f_{jj''}(\vec{k})\Sigma_{j''j'}(\vec{k})\},
\end{aligned} \tag{B2}$$

and a similar equation for $f_{ss'}(\vec{k})$. The Luttinger Hamiltonian for the valence bands in the basis $\{j\}=(3/2,-1/2,1/2,-3/2)$ with basis functions defined in Ref. [52] reads (see also [53–56])

$$\mathcal{H}=\begin{pmatrix} H_{hh} & c^* & 0 & 0\\ c & H_{lh} & 0 & 0\\ 0 & 0 & H_{lh} & c^*\\ 0 & 0 & c & H_{hh}\end{pmatrix}. \tag{B3}$$

The energy renormalizations are given by

$$\Sigma_{aa'}(\vec{k})=-\sum_{\vec{q}}V(\vec{q})f_{aa'}(\vec{k}+\vec{q}) \tag{B4}$$

(with $a=s$ or j) and the renormalized dipole energy is

$$\Omega_{sj}^{(ren)}(\vec{k})=\Omega_{sj}(\vec{k})+\sum_{\vec{q}}V(\vec{q})P_{sj}(\vec{k}+\vec{q}), \quad \Omega_{sj}=\vec{\mu}_{sj}\cdot\vec{E}. \tag{B5}$$

The dipole energy is $\Omega_{sj}(\vec{k})$ and the electric field vector is given by Eq. (A14). The dipole matrix elements $\vec{\mu}_{sj}$ contain the information of optical selection rules. Using the transformation between circular ($\vec{e}_{\pm}$) and Cartesian ($\vec{e}_{x/y}$) unit vectors

$$\vec{e}_{\pm}=\mp\frac{1}{\sqrt{2}}\,(\vec{e}_x\pm i\vec{e}_y), \tag{B6}$$

one can write the dipole matrix elements [67] as

$$\begin{aligned}\vec{\mu}_{1/2,3/2}&=\sqrt{3}\vec{\mu}_{-1/2,1/2}=-\mu\vec{e}_+,\\ \vec{\mu}_{-1/2,-3/2}&=\sqrt{3}\vec{\mu}_{1/2,-1/2}=-\mu\vec{e}_-.\end{aligned} \tag{B7}$$

The total polarization density is given by

$$\vec{P}_{QW}=\frac{2}{L^2}\sum_{\vec{k},s,j}\vec{\mu}_{sj}^{*}P_{sj}(\vec{k}), \tag{B8}$$

see Eq. (A15), where the spatial dependence of $\vec{P}_{QW}$ follows the spatial dependence of $P_{sj}(\vec{k})$ and L^2 denotes the quantum well surface.

Before we proceed further, we note that for cavities with small losses and for large enough hh-lh splitting, only the hh gain contributes to the cavity dynamics. Therefore we can simplify the set of Eqs. (B1)–(B2) and consider *only* populations of heavy holes and polarizations between conduction and heavy-hole bands corresponding to both subsystems. However, one is allowed to do this only in the basis where hh and lh bands are well defined (i.e., there is no crossing between bands), that is in the basis where the Luttinger Hamiltonian (B3) is diagonal [58].

The elements of the unitary transformation matrix $\mathcal{U}\equiv\{u\}_{ij}$, $i,j=1,\ldots,4$, that diagonalizes the Luttinger Hamiltonian are given by $u_{11}=(H_{lh}-E_{hh})/N_{hh}$, $u_{22}=(E_{lh}-H_{hh})/N_{lh}$, $u_{12}=c^*/N_{lh}$, $u_{21}=-c/N_{hh}$, and $u_{44}=u_{11}$, $u_{33}=u_{22}$, $u_{34}=u_{21}^*$, $u_{43}=u_{12}^*$, with other elements being 0. Denoting $u=u_{11}$ and $v=u_{21}$ and using the unitarity property of $\mathcal{U}$ one can write

$$\begin{aligned}\mathcal{U}&=\begin{pmatrix}\mathcal{U}_{1/2} & 0\\ 0 & \mathcal{U}_{-1/2}\end{pmatrix},\quad \mathcal{U}_{1/2}=\begin{pmatrix}u & -v^*\\ v & u\end{pmatrix},\\ \mathcal{U}_{-1/2}&=\begin{pmatrix}u & v^*\\ -v & u\end{pmatrix}.\end{aligned} \tag{B9}$$

The expressions defining the dependence of u, v, E_{hh}, E_{lh}, H_{hh}, H_{lh}, and c on the in-plane momentum $\vec{k}$ are given by Eqs. (13)–(15). The transformations to the basis where $\mathcal{H}$ is diagonal (denoted by $\tilde{}$) are given by

$$\mathcal{U}^{-1}\mathcal{H}\mathcal{U}=\tilde{\mathcal{H}},\quad \mathcal{U}^{-1}\hat{f}^h\mathcal{U}=\tilde{f}^h,\quad P=\mathcal{U}\tilde{P},\quad \Omega=\mathcal{U}\tilde{\Omega}, \tag{B10}$$

and $\tilde{\mathcal{H}}_{3/2,3/2}=E_{hh}(\vec{k})=\tilde{\mathcal{H}}_{-3/2,-3/2}$, $\tilde{\mathcal{H}}_{1/2,1/2}=E_{lh}(\vec{k})=\tilde{\mathcal{H}}_{-1/2,-1/2}$.

These transformations can be simplified if one neglects transitions between the light hole and the conduction bands, i.e.,

$$\begin{aligned}\tilde{P}_{1/2,-1/2}&=0=\tilde{P}_{-1/2,1/2},\\ \tilde{f}_{-1/2,-1/2}&=\tilde{f}_{-1/2,3/2}=\tilde{f}_{3/2,-1/2}=0,\\ \tilde{f}_{1/2,1/2}&=\tilde{f}_{1/2,-3/2}=\tilde{f}_{-3/2,1/2}=0.\end{aligned} \tag{B11}$$

This yields the polarizations in both spin subsystems as

$$\begin{aligned}&P_{1/2,3/2}=u\tilde{P}_{1/2,3/2},\quad P_{1/2,-3/2}=v\tilde{P}_{1/2,3/2},\\ &P_{-1/2,1/2}=v^*\tilde{P}_{-1/2,-3/2},\quad P_{-1/2,-3/2}=u\tilde{P}_{-1/2,-3/2}.\end{aligned} \tag{B12}$$

The inverse transformation reads

$$\begin{aligned}\tilde{P}_{1/2,3/2}&=uP_{1/2,3/2}+v^*P_{1/2,-1/2},\\ \tilde{P}_{-1/2,-3/2}&=vP_{-1/2,1/2}+uP_{-1/2,-3/2}.\end{aligned} \tag{B13}$$

Similar relationships hold for the dipole energies $\Omega_{\pm1/2\pm3/2}$ and $\tilde{\Omega}_{\pm1/2,\pm3/2}$. As far as notation used here is concerned, one should be aware that even within the spherical approximation used here the dipole moments are given in the basis where the Luttinger Hamiltonian is nondiagonal, and only in this basis the indices $i=\pm1/2,\pm3/2$ can be understood as effective magnetic quantum numbers corresponding to the total angular momentum quantum number 3/2 of electrons in the valence band. In the diagonalized basis the wave functions describing hh and lh bands are superpositions with weighting factors determined by relations (B10). In this basis we use the subscript $\pm3/2$ to indicate that only hh contribution are considered.

2. Adiabatic elimination of microscopic polarizations

Consistently with the rotating wave approximation performed on the electric field amplitude in Appendix A, we eliminate the fast oscillating terms in Eqs. (B1); that is, we consider only the terms with $e^{-i\omega_0 t}$ time dependence. Since we are mainly interested in the steady-state characteristics of the lasers, we can adiabatically eliminate the time derivative of the slowly varying polarization amplitude in Eq. (B1). Transforming the resulting equation into the basis where the Luttinger Hamiltonian is diagonal, one obtains

$$\begin{aligned}&\tilde{P}_{1/2,3/2}(\vec{k})\left(-\frac{i\hbar}{T_2}+\varepsilon_k^s+E_{hh}(\vec{k})-\Sigma_{1/2}(\vec{k})-\hbar\omega_0\right)\\ &\quad=(1-f^e_{1/2,1/2}(\vec{k})-\tilde{f}^h_{3/2,3/2}(\vec{k}))\Bigg[\tilde{\Omega}_{1/2,3/2}(\vec{k})\\ &\qquad+\sum_{\vec{q}}V(\vec{q})(u(\vec{k})u(\vec{k}+\vec{q})\\ &\qquad+v^*(\vec{k})v(\vec{k}+\vec{q}))\tilde{P}_{1/2,3/2}(\vec{k}+\vec{q})\Bigg]\end{aligned} \tag{B14}$$

and

$$\tilde{P}_{-1/2,-3/2}(\vec{k})\left(-\frac{i\hbar}{T_2}+\varepsilon_k^s+E_{hh}(\vec{k})-\Sigma_{-1/2}(\vec{k})-\hbar\omega_0\right)$$
$$=(1-f^{e}_{-1/2,-1/2}(\vec{k})-\tilde{f}^{h}_{-3/2,-3/2}(\vec{k}))\Bigg[\tilde{\Omega}_{-1/2,-3/2}(\vec{k})$$
$$+\sum_{\vec{q}} V(\vec{q})(u(\vec{k})u(\vec{k}+\vec{q})+v(\vec{k})v^*(\vec{k}+\vec{q}))$$
$$\times\tilde{P}_{-1/2,-3/2}(\vec{k}+\vec{q})\Bigg],$$

where the band-gap renormalization $\Sigma_{\pm 1/2}(\vec{k})$ is given by Eq. (10). One can see that due to coupling of different $\vec{k}$ states via the Coulomb interaction, the solution of Eq. (B14) cannot be written down in an explicit form. One way to solve this problem is by using the Padé approximation, similarly to the one presented in Ref. [57] for the case of a two-band model. In zeroth order in the Coulomb potential one obtains the well-known free-carrier steady-state solution for the microscopic polarization

$$\tilde{P}^{(0)}_{\pm 1/2,\pm 3/2}(\vec{k})=\mathcal{F}_{\pm 1/2}(\vec{k})\tilde{\Omega}_{\pm 1/2,\pm 3/2}(\vec{k}), \tag{B15}$$

where $\mathcal{F}_{\pm 1/2}(\vec{k})$ is a free-carrier factor given by Eq. (8). A suitable 0–1 Padé approximation for the microscopic polarization $\tilde{P}_{\pm 1/2,\pm 3/2}(\vec{k})$ is

$$\tilde{P}^{(Pade)}_{\pm 1/2,\pm 3/2}(\vec{k})=\frac{\mathcal{F}_{\pm 1/2}(\vec{k})}{1-\mathcal{G}_{\pm 1/2}(\mathcal{F}_{\pm 1/2};\vec{k})}\tilde{\Omega}_{\pm 1/2,\pm 3/2}(\vec{k}), \tag{B16}$$

where $\mathcal{G}_{\pm 1/2}(\mathcal{F}_{\pm 1/2};\vec{k})$ is a local-field correction factor given by Eq. (9). In deriving (B16) we used the approximation

$$\mathcal{G}_{\pm 1/2}(\mathcal{F}_{\pm 1/2}\tilde{\Omega}_{\pm 1/2,\pm 3/2};\vec{k})\approx\tilde{\Omega}_{\pm 1/2,\pm 3/2}(\vec{k})\mathcal{G}_{\pm 1/2}(\mathcal{F}_{\pm 1/2};\vec{k}). \tag{B17}$$

Note, that the steady-state solution given by Eq. (B16) provides an explicit relationship between microscopic polarization and dipole energy $\Omega_{\pm 1/2,\pm 3/2}$, which is related to the electric field vector $\vec{E}$ by Eq. (B5). Also, since the basis vectors of the circular and Cartesian coordinate system transform according to Eq. (B6), the components of electric fields and macroscopic polarizations in these two coordinate systems are related by

$$E_{\pm}(\vec{r},t)=\frac{1}{\sqrt{2}}\left[\mp e_x^{(tot)}(\vec{r},t)+ie_y^{(tot)}(\vec{r},t)\right], \tag{B18}$$

$$P_{\pm}(\vec{r},t)=\frac{1}{\sqrt{2}}\left[\mp P_x(\vec{r},t)+iP_y(\vec{r},t)\right],$$

with $e_{x/y}^{(tot)}$ and $P_{x/y}$ being the x/y components of the electric field of hybrid modes (A21) and macroscopic polarization, respectively. The relationship (B18) applied to both the electric field and the total polarization density (B8) allows us to identify the elements of the susceptibility tensor $\hat{\chi}_{QW}(\omega_0)$ [see Eq. (A13)] given by Eq. (11).

Note that the spatial dependence of the susceptibility tensor $\hat{\chi}_{QW}$ is determined by the spatial profile of functions $\mathcal{F}_{\pm 1/2}$ and $\mathcal{G}_{\pm 1/2}(\mathcal{F}_{\pm 1/2};\vec{k})$, and therefore by the spatial dependence of carrier distribution functions. This problem will be addressed in Appendix B 3. Note also that if the hh-lh splitting $\Delta_{hl}\to\infty$, then $u\to 1$ and $v\to 0$, and one obtains the model without band-mixing effects.

3. Calculation of stimulated emission within the Padé approximation

In order to calculate the stimulated emission contribution to the equations describing the carrier dynamics inside the QW, we eliminate the light-hole contribution to the modal gain in a similar fashion as it has been done for the microscopic polarizations. We transform Eqs. (B2) into the basis where the Luttinger Hamiltonian is diagonal and impose the condition given by Eq. (B11) for the microscopic polarizations and density distributions. We use the solution given by Eq. (B16) for the polarizations between heavy-hole and conduction bands. After straightforward but lengthy calculations one obtains the following expressions for the heavy-hole gain contributions:

$$\left(\frac{d}{dt}\tilde{f}^{h}_{\pm 3/2,\pm 3/2}(\vec{k};r)\right)_s$$
$$=\frac{|\mu|^2}{2\hbar}\,\mathrm{Im}\Bigg[\left[1+\mathcal{G}^*_{\pm 1/2}(\mathcal{F}_{\pm 1/2};-\vec{k})\right]$$
$$\times\frac{\mathcal{F}_{\pm 1/2}(-\vec{k})}{1-\mathcal{G}_{\pm 1/2}(\mathcal{F}_{\pm 1/2};-\vec{k})}\left[\chi_{QW}^{xx\pm}|e_x^{(tot)}|^2\right.$$
$$+\chi_{QW}^{xy\pm}(e_x^{(tot)})^*e_y^{(tot)}+\chi_{QW}^{yx\pm}e_x^{(tot)}(e_y^{(tot)})^*$$
$$\left.+\chi_{QW}^{yy\pm}|e_y^{(tot)}|^2\right]\Bigg], \tag{B19}$$

and

$$\left(\frac{d}{dt}f^{e}_{\pm 1/2,\pm 1/2}(\vec{k};r)\right)_s=\left(\frac{d}{dt}\tilde{f}^{h}_{\pm 3/2,\pm 3/2}(\vec{k};r)\right)_s,$$

where $e_x^{(tot)}$ and $e_y^{(tot)}$ are the x and y components of the total electric field $\vec{e}^{(tot)}$ defined by Eq. (A21), but including both forward and backward propagating fields. Note that the carrier distributions resulting from Eq. (B19) are explicitly related to radially dependent electric fields, and therefore they should be considered as Wigner functions. However, as mentioned in Appendix A 3, we neglect spatial hole burning effects by spatially averaging Eq. (B19) over the cavity cross

section. Thus, performing the integration over $\int d\mathcal{A}$, normalizing over the surface of the QW and introducing spatially averaged carrier distributions, one obtains the time evolution equations (7). For simplicity of notation, we use the same symbol f as in Eq. (B19) to denote the averaged carrier distributions. The modal field overlap factor is given by

$$\Gamma_R = \frac{2}{R^2} \int_0^R r f_1(r) f_2(r) dr, \tag{B20}$$

where $f_1(r)$ and $f_2(r)$ are defined in Eq. (A20).

[1] W. W. Chow *et al.*, IEEE J. Quantum Electron. **33**, 1810 (1997).
[2] C. J. Chang-Hasnain *et al.*, IEEE J. Quantum Electron. **27**, 1402 (1991).
[3] S. Jiang *et al.*, Appl. Phys. Lett. **63**, 3545 (1993).
[4] J. E. Epler *et al.*, Appl. Phys. Lett. **69**, 722 (1996).
[5] J. Martin-Regalado, J. L. A. Chilla, J. J. Rocca, and P. Brusenbach, Appl. Phys. Lett. **70**, 3350 (1997).
[6] M. P. van Exter, A. Al-Remawi, and J. P. Woerdman, Phys. Rev. Lett. **80**, 4875 (1998).
[7] K. D. Choquette and R. E. Leibenguth, IEEE Photonics Technol. Lett. **6**, 40 (1994).
[8] B. Gayral *et al.*, Appl. Phys. Lett. **72**, 1421 (1998).
[9] S. J. Schablitsky, L. Zhuang, R. C. Shi, and S. Y. Chou, Appl. Phys. Lett. **69**, 7 (1996).
[10] T. Mukaihara *et al.*, IEEE J. Sel. Top. Quantum Electron. **1**, 667 (1995).
[11] P. Dowd *et al.*, Electron. Lett. **1997**, 1315 (1997).
[12] H. Y. Chu, B.-S. Yoo, M. S. Park, and H.-H. Park, IEEE Photonics Technol. Lett. **9**, 1066 (1997).
[13] A. Chavez-Pirson, H. Ando, H. Saito, and H. Kanbe, Appl. Phys. Lett. **62**, 3082 (1993).
[14] C. L. Chua, R. L. Thornton, D. W. Treat, and R. M. Donaldson, Appl. Phys. Lett. **73**, 1631 (1998).
[15] A. K. Dutta and K. Kasahara, Solid-State Electron. **42**, 907 (1998).
[16] K. D. Choquette, J. R. P. Schneider, and J. A. Lott, Opt. Lett. **19**, 969 (1994).
[17] A. Chavez-Pirson, H. Ando, H. Saito, and H. Kanbe, Appl. Phys. Lett. **64**, 1759 (1994).
[18] H. Saito, K. Nishi, S. Sugou, and Y. Sugimoto, Appl. Phys. Lett. **71**, 590 (1997).
[19] K. D. Choquette, D. A. Richie, and R. E. Leibenguth, Appl. Phys. Lett. **64**, 2062 (1994).
[20] K. D. Choquette, R. P. Schneider, K. L. Lear, and R. E. Leibenguth, IEEE J. Sel. Top. Quantum Electron. **1**, 661 (1995).
[21] A. K. J. V. Doorn, M. P. V. Exter, and J. P. Woerdman, Appl. Phys. Lett. **69**, 1041 (1996).
[22] A. K. J. V. Doorn, M. P. V. Exter, and J. P. Woerdman, Appl. Phys. Lett. **69**, 3635 (1996).
[23] A. K. J. V. Doorn, M. P. V. Exter, A. M. V. D. Lee, and J. P. Woerdman, Phys. Rev. A **55**, 1473 (1997).
[24] M. San Miguel, Q. Feng, and J. V. Moloney, Phys. Rev. A **52**, 1728 (1995).
[25] J. Martin-Regalado, F. Prati, M. S. Miguel, and N. B. Abraham, IEEE J. Quantum Electron. **33**, 765 (1997).
[26] C. Serrat *et al.*, Phys. Rev. A **53**, R3731 (1996).
[27] M. Travagnin, M. P. van Exter, A. K. van Doorn, and J. P. Woerdman, Phys. Rev. A **54**, 1647 (1996).
[28] M. Travagnin, M. P. van Exter, and J. P. Woerdman, Phys. Rev. A **56**, 1497 (1997).
[29] H. F. Hofmann and O. Hess, Phys. Rev. A **56**, 868 (1997).
[30] H. van der Lem and D. Lenstra, Opt. Lett. **22**, 1698 (1997).
[31] M. P. van Exter, R. F. M. Hendriks, and J. P. Woerdman, Phys. Rev. A **57**, 2080 (1998).
[32] J. Martin-Regalado *et al.*, Quantum Semiclassic. Opt. **9**, 713 (1997).
[33] A. Valle, L. Pesquera, and K. A. Shore, IEEE Photonics Technol. Lett. **9**, 557 (1997).
[34] A. Valle *et al.*, in *Proceedings of the SPIE Conference: Physics and Simulation of Optoelectronic Devices VI*, edited by M. Osinki, P. Blood, and A. Tshibashi (The International Society for Optical Engineering, Bellingham, WA, 1998), Vol. 3283, pp. 280–291.
[35] H. Haug and S. W. Koch, Phys. Rev. A **39**, 1887 (1989).
[36] L. Fratta, M. S. thesis, University of Milano, 1996; F. Prati, F. Fratta, and M. Travagnin (unpublished).
[37] F. Jahnke and S. W. Koch, Phys. Rev. A **52**, 1712 (1995).
[38] F. Jahnke, K. Henneberger, W. Schaefer, and S. W. Koch, J. Opt. Soc. Am. B **10**, 2394 (1993).
[39] O. Hess, S. W. Koch, and J. V. Moloney, IEEE J. Quantum Electron. **31**, 35 (1995).
[40] O. Hess, Opt. Express **2**, 424 (1998).
[41] C. Z. Ning, R. A. Indik, and J. V. Moloney, J. Opt. Soc. Am. B **12**, 1993 (1995).
[42] T. Roessler *et al.*, Phys. Rev. A **58**, 3279 (1998).
[43] R. F. M. Hendriks *et al.*, IEEE J. Quantum Electron. **34**, 1455 (1998).
[44] C. C. Lin and D. G. Deppe, J. Lightwave Technol. **13**, 575 (1995).
[45] B. Demeulenaere, D. DeZutter, and R. Baets, IEE Proc.: Optoelectron. **143**, 221 (1996).
[46] M. J. Noble, J. P. Loehr, and J. A. Lott, IEEE J. Quantum Electron. **34**, 1890 (1998).
[47] D. Burak and R. Binder, IEEE J. Quantum Electron. **33**, 1205 (1997).
[48] D. Burak and R. Binder, Appl. Phys. Lett. **72**, 891 (1998).
[49] M. J. Noble, J. P. Loehr, and J. A. Lott, IEEE J. Quantum Electron. **34**, 2327 (1998).
[50] G. Liu *et al.*, Appl. Phys. Lett. **73**, 726 (1998).
[51] D. Burak and R. Binder, in *Proceedings of the SPIE Conference: Physics and Simulation of Optoelectronic Devices VI* (Ref. [34]), pp. 269–279.
[52] F. H. Pollak, in *Strained-Layer Superlattices: Physics*, Vol. 32 of Semiconductors and Semimetals, edited by T. T. Pearsall (Academic, New York, 1990), pp. 17–53.
[53] H. Shen *et al.*, Phys. Rev. B **47**, 13 933 (1993).

[54] M. Wraback *et al.*, Surf. Sci. **305**, 238 (1994).
[55] M. Wraback *et al.*, Phys. Rev. Lett. **74**, 1466 (1995).
[56] H. Shen *et al.*, IEEE Photonics Technol. Lett. **6**, 700 (1994).
[57] W. W. Chow, S. W. Koch, and M. Sargent, *Semiconductor-Laser Physics* (Springer-Verlag, Berlin, 1994).
[58] R. Binder and S. Koch, Prog. Quantum Electron. **19**, 307 (1995).
[59] R. Binder, Phys. Rev. Lett. **78**, 4466 (1997).
[60] D. W. Jenkins, J. Appl. Phys. **68**, 1848 (1990).
[61] S. L. Chuang, *Physics of Optoelectronic Devices* (Wiley, New York, 1995).
[62] J. P. Loehr, *Physics of Strained Quantum Well Lasers* (Kluwer Academic, Boston, 1998).
[63] M. Travagnin, Phys. Rev. A **56**, 4094 (1997).
[64] M. Travagnin, Quantum Semiclassic. Opt. **10**, 223 (1997).
[65] M. P. van Exter, M. B. Willemsen, and J. P. Woerdman, Phys. Rev. A **58**, 4191 (1998).
[66] A. W. Snyder and J. D. Love, *Optical Waveguide Theory* (Chapman and Hall, New York, 1992).
[67] *Optical Orientation*, edited by F. Meier and B. Zakharchenya (North-Holland, Amsterdam, 1984).